Optimal energy growth and optimal control in swept Hiemenz flow

Alan Guégan, Peter Schmid, Patrick Huerre

J. Fluid Mech. (2006), *vol.* 566, *pp.* 11–45.
doi:10.1017/S0022112006001303 Printed in the United Kingdom

Optimal energy growth and optimal control in swept Hiemenz flow

By ALAN GUÉGAN[1], PETER J. SCHMID[1,2] AND PATRICK HUERRE[1]

[1]Laboratoire d'Hydrodynamique (LadHyX), CNRS-École Polytechnique, F-91128 Palaiseau, France

[2]Department of Applied Mathematics, University of Washington, Seattle, WA 98195-2420, USA

(Received 7 January 2005 and in revised form 16 February 2006)

The objective of the study is first to examine the optimal transient growth of Görtler–Hämmerlin perturbations in swept Hiemenz flow. This configuration constitutes a model of the flow in the attachment-line boundary layer at the leading-edge of swept wings. The optimal blowing and suction at the wall which minimizes the energy of the optimal perturbations is then determined. An adjoint-based optimization procedure applicable to both problems is devised, which relies on the maximization or minimization of a suitable objective functional. The variational analysis is carried out in the framework of the set of linear partial differential equations governing the chordwise and wall-normal velocity fluctuations. Energy amplifications of up to three orders of magnitude are achieved at low spanwise wavenumbers ($k \sim 0.1$) and large sweep Reynolds number ($Re \sim 2000$). Optimal perturbations consist of spanwise travelling chordwise vortices, with a vorticity distribution which is inclined against the sweep. Transient growth arises from the tilting of the vorticity distribution by the spanwise shear via a two-dimensional Orr mechanism acting in the basic flow dividing plane. Two distinct regimes have been identified: for $k \lesssim 0.25$, vortex dipoles are formed which induce large spanwise perturbation velocities; for $k \gtrsim 0.25$, dipoles are not observed and only the Orr mechanism remains active. The optimal wall blowing control yields for instance an 80 % decrease of the maximum perturbation kinetic energy reached by optimal disturbances at $Re = 550$ and $k = 0.25$. The optimal wall blowing pattern consists of spanwise travelling waves which follow the naturally occurring vortices and qualitatively act in the same manner as a more simple constant gain feedback control strategy.

1. Introduction

Fundamental studies of hydrodynamic instabilities in boundary layers have been motivated by the need to suppress or delay transition to turbulence over aircraft lift-generating devices. Most classical investigations have been concerned with the boundary layers on the upper and lower surfaces when the flow may be regarded as weakly non-parallel and disturbances governed by the Orr–Sommerfeld equation or any of its extensions. Relatively little attention has been given to the highly three-dimensional region at the leading-edge. The main objective of the present study is to determine the optimal energy growth sustainable by disturbances in the swept-attachment line boundary layer otherwise known as swept Hiemenz flow. An optimal control strategy based on blowing and suction at the wall is then devised in order to quench these perturbations.

Early experimental studies of swept wing attachment-line boundary layers (Gregory 1960; Gaster 1967; Cumpsty & Head 1969; Pfenninger & Bacon 1969; Pfenninger 1977) were motivated by the need to keep the flow in this region laminar, in order to prevent premature transition downstream over the wing surface. Crossflow instabilities appearing away from the attachment line were then thought to be responsible for early transition. See Koch, Bertolotti, Stolte & Hein (2000) for a theoretical and numerical study of crossflow vortices in three-dimensional boundary layers and their secondary instability. Poll (1979) emphasized that instabilities at the attachment line, intrinsic to the leading-edge boundary layer, could also play a significant role in this process. The present investigation focuses on the naturally occurring instability originating at the attachment-line and its control.

A satisfactory model of the steady flow near the attachment-line is given by the Hiemenz (1911) stagnation-point solution over which is superimposed a spanwise velocity component. The linear instability properties of this highly non-parallel basic flow have been the subject of conflicting statements regarding the assumed behaviour of fluctuations outside the boundary layer. The main conclusions may be summarized as follows.

Under the so-called Görtler (1955)–Hämmerlin (1955) separation of variables assumption (2.5) and exponential decay of the perturbations in the wall-normal direction, Hiemenz stagnation flow without sweep was conclusively demonstrated to be linearly stable by Wilson & Gladwell (1978). Lyell & Huerre (1985) showed that the previously suspected centrifugal instability mechanism was indeed present, but too weak to counteract the stabilizing effect of viscous diffusion. They further concluded that there was the possibility of a finite-amplitude instability on the basis of a highly truncated Galerkin model of the nonlinear dynamics. The direct numerical simulations of Spalart (1988) failed to detect any evidence for such a nonlinear instability in pure Hiemenz flow. The restrictive Görtler–Hämmerlin assumption was first relaxed in the study of Brattkus & Davis (1991) by expanding perturbations in series of Hermite polynomials along the chordwise direction. Algebraically decaying disturbances in the wall-normal direction, which are associated to the continuous spectrum, were shown by Dhanak & Stuart (1995) to arise from fluctuations forced from outside the boundary layer.

The presence of sweep significantly modifies the above results. According to Hall, Malik & Poll (1984), who led a study under the Görtler–Hämmerlin assumption, there exists a critical value $Re_c = 583.1$ of the sweep Reynolds number (defined in § 2) above which swept Hiemenz flow becomes linearly unstable. Sufficiently strong steady wall suction makes the flow stable while blowing has a destabilizing effect. Furthermore, a weakly nonlinear analysis (Hall & Malik 1986) reveals the bifurcation to be subcritical close to Re_c. This result is in qualitative agreement with the direct numerical simulations of Spalart (1988) for swept Hiemenz flow where subcritical turbulent states were observed below Re_c. Lin & Malik (1996), Theofillis *et al.* (2003) and Obrist & Schmid (2003*a*) have extended the linear analysis to more general chordwise polynomial expansions in the same spirit as Brattkus & Davis (1991). The Görtler–Hämmerlin modes are then found to be the least stable. According to the direct numerical simulations of Joslin (1995), the nonlinear spatial evolution of two-dimensional and three-dimensional disturbances is in line with the temporal instability results of Hall & Malik (1986). Swept Hiemenz flow indeed becomes linearly unstable at sufficiently large Reynolds numbers and wall suction strongly stabilizes the flow. However, no definite evidence for the subcritical instability was found. Theofilis (1998) carried out a comprehensive comparison between simulations of the full nonlinear equations and the linear instability analysis, both under the Görtler–Hämmerlin

separation of variable assumption. Excellent agreement was obtained in the supercritical range. Again, no finite-amplitude subcritical instability was clearly exhibited, which was ascribed to the restrictive nature of the Görtler–Hämmerlin assumption.

It is now well established that classical linear instability analyses must be complemented with a study of the transient growth properties of non-modal perturbations (Gustavsson 1991; Butler & Farrell 1992; Trefethen *et al.* 1993). For a general account of the underlying theoretical framework, see Schmid & Henningson (2001). In the specific context of swept Hiemenz flow, Obrist & Schmid (2003*b*) demonstrated that, within the limitations of a finite eigenfunction basis, Görtler–Hämmerlin perturbations could support an energy amplification of the order of 100 in the linearly stable regime, both at low and high spanwise wavenumbers, provided that the Reynolds number is large enough. The investigation was carried out by resorting to a standard singular value decomposition method applied to the gain matrix over a finite time interval. In the present study, the issue of transient temporal growth is examined anew by implementing an adjoint-based optimization formulation (see, for instance, Gunzburger 1997) in order to determine the perturbation of maximum growth. A similar methodology has been used in Andersson, Berggren & Henningson (1999) and Luchini (2000) to examine optimal streamwise amplification in the Blasius boundary layer. The analysis developed in § 3 is inspired by the procedure proposed by Corbett & Bottaro (2001*a*) to identify optimal disturbances in swept boundary layers in a temporal setting.

For an assessment of the current status of laminar flow control technology in an aeronautical context, see Joslin (1998) and Gad-el-Hak (2000). At a more fundamental level, applications of control theory (Abergel & Témam 1990) to the delay of boundary-layer transition have recently led to very encouraging results. For general accounts and reviews of the applications of control theory to transitional or turbulent flows, see Gunzburger (1997), Lumley & Blossey (1998) and Bewley (2001) among others. We restrict here the discussion to studies that are directly relevant to this investigation, namely optimal control methodologies involving adjoint formulations in a continuous setting and applied to boundary-layer transition. More specifically, the optimal control problem for perturbations within the flow is viewed as the minimization of an objective functional involving a measure of the perturbation energy, under the constraint that disturbances satisfy for instance the linear Navier–Stokes equations (Gunzburger 1997; Joslin *et al.* 1997). For that purpose, an iterative method based on the calculation of the gradient of the objective functional with respect to the control variables, e.g. wall blowing/suction, is implemented in order to reach a local minimum in function space. The gradient vector of the objective functional may conveniently be expressed in terms of an adjoint state which is a solution of an adjoint system of equations and boundary conditions. Such a formulation is carried out in the context of continuous linear instability partial differential equations. Discretization is only performed *a posteriori* in order to effectively solve numerically the direct and adjoint systems. Other formulations, which are not considered here, involve instead an *a priori* discretization before resorting to an optimization scheme. Such approaches are appropriate when the evaluation of the gradient of the objective functional in terms of the adjoint is numerically delicate.

Another issue concerns the so-called off-line versus on-line formulation of control problems. In the present investigation, the optimization is performed off-line, i.e. the optimal control is determined once and for all for a given initial state. By contrast, on-line formulations rely on the determination of feedback laws. The procedure then often involves solving a Riccati equation, thereby leading to a gain matrix

directly relating the control to the state of the system, as extensively reviewed in Bewley (2001). Such approaches lead to efficient feedback control laws in plane channel flow, as demonstrated for a single Fourier mode in two dimensions by Joshi, Speyer & Kim (1997) and in three dimensions by Bewley & Liu (1998). Högberg, Bewley & Henningson (2003) successfully generalized the procedure to arbitrary initial disturbances in physical space. A similar framework has been adopted by Högberg & Henningson (2002) to control various unstable perturbations in spatially evolving three-dimensional boundary layers.

In the continuous framework and following the general adjoint-based optimization methodology put forward by Joslin *et al.* (1997), Cathalifaud & Luchini (2000) determined the optimal streamwise distribution of wall blowing and suction which minimizes the perturbation energy of the incoming disturbance of maximum growth in two-dimensional boundary layers on a flat or curved plate. Walther, Airiau & Bottaro (2001) implemented a similar formulation to compute the optimal wall transpiration capable of quenching the streamwise development of two-dimensional Tollmien–Schlichting waves in a spatially developing boundary layer. The evolution of instability waves was assumed to be governed by the linear parabolic stability equations. Several orders of magnitude reductions in perturbation energy were achieved. A similar methodology has been applied by Pralits, Hanifi & Henningson (2002) to control the growth of various classes of disturbances in three-dimensional boundary layers. A sophisticated generalization of this type of approach has been proposed by Bewley, Moin & Temam (2001) in order to control turbulence in direct numerical simulations of plane channel flow at Reynolds numbers of 1712 and 3247. A so-called 'receding-horizon' predictive control strategy was devised, in which the optimal blowing/suction control sequence is calculated on a given short time horizon, the flow being frozen. This short-time optimal control is then applied to advance the flow during a fraction of this time horizon. This process is repeated until the flow is fully relaminarized. The optimal control framework has also been applied in a linear setting by Corbett & Bottaro (2001*b*) to attenuate via unsteady suction and blowing the optimal temporally evolving perturbation in swept boundary layers calculated by Corbett & Bottaro (2001*a*). The perturbation kinetic energy amplification was shown to be reduced by an order of magnitude in accelerated boundary layers.

The present investigation differs from previous optimal control analyses in the following aspects. The optimization scheme, used for the determination of both the optimal disturbance and the optimal suction/blowing control sequence is developed for a highly non-parallel basic flow, instead of the strictly parallel plane Poiseuille flow or weakly non-parallel boundary layers. Disturbances are assumed to satisfy the Görtler–Hämmerlin separation of variable assumption (2.5). As in previous studies discussed above, the optimization procedure is carried out in a continuous setting on a reduced set of linear partial differential equations governing the evolution of the chordwise (u) and wall-normal (v) velocity perturbations, in the same spirit as, for instance, Corbett & Bottaro (2001*a*, *b*). However, it is argued that the reduction to a $u-v$ formulation requires a non-trivial adaptation of existing approaches, namely, the introduction of a suitable set of scalar products. As a result, the different components of the gradient of the objective functional are directly accessible in a reduced $u-v$ setting. Gradient algorithms are then readily available to home in on a local optimum of the objective function. Finally, a new physical mechanism responsible for the growth of non-modal perturbations is identified which also provides a qualitative explanation for the efficiency of the control.

The paper is organized as follows. The basic flow and the Görtler–Hämmerlin linear perturbation model are introduced and defined in § 2. The optimization approach

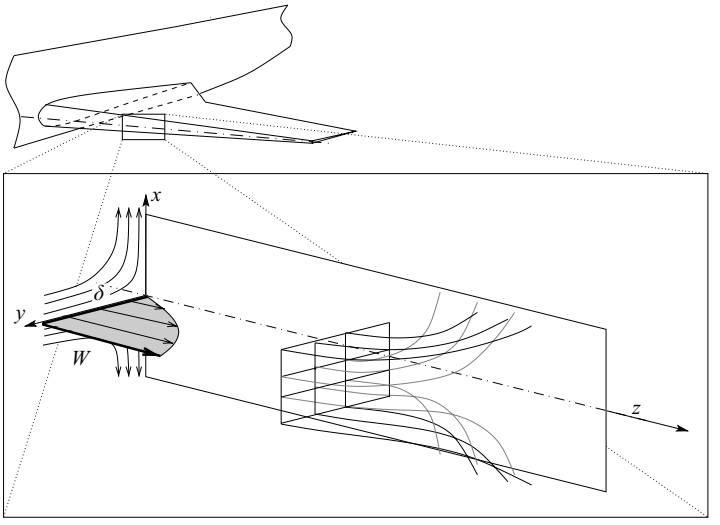

FIGURE 1. Sketch of the leading-edge boundary layer forming near the stagnation region of a swept wing. The inset further simplifies the flow geometry by neglecting curvature effects of the leading edge. Both the basic profile and streamlines are displayed.

common to the optimal perturbation and optimal control analyses is detailed in § 3. Application to swept Hiemenz flow and numerical issues are addressed in § 4. Section 5 provides the underlying physical mechanisms at low and high spanwise wavenumbers-respectively. Optimal control is examined in § 6 and compared with a constant gain feedback control law reminiscent of opposition control. A summary of the main findings is given in § 7 and additional remarks are made regarding the particular features of the growth mechanism, as compared to its classical boundary-layer counterpart.

2. Linear perturbation model

As a uniform flow impinges on the swept leading edge of an airfoil (figure 1), or any blunt body, an attachment-line boundary layer forms in the vicinity of the stagnation line. In the neighbourhood of the stagnation line, the leading edge can be modelled locally by a flat wall perpendicular to the main stream. Cartesian coordinates (x, y, z) are then introduced where the normal coordinate direction y is perpendicular to the wall and points upstream, z and x denote the spanwise and chordwise direction, respectively (figure 1), and the base flow divides symmetrically over each side of the (y, z) dividing plane. This model, known as swept Hiemenz flow, provides a widely accepted description of the steady flow near the stagnation region.

The Reynolds number of the flow is based on the free-stream sweep velocity W_∞, the kinematic viscosity ν and the length scale $\delta = (\nu/S)^{1/2}$, with $S = (\mathrm{d}U/\mathrm{d}x)_{y\to\infty}$ denoting the strain rate of the irrotational outer flow and U the chordwise velocity of the base flow. The Reynolds number thus defined,

$$Re = \frac{W_\infty \delta}{\nu}, \tag{2.1}$$

represents a measure of the sweep angle where $Re = 0$ corresponds to unswept Hiemenz flow. The Navier-Stokes equations are non-dimensionalized based on the length scale δ and the velocity scale W_∞.

The base flow (U, V, W) is assumed to be steady and independent of the spanwise z-coordinate. Following Hiemenz (1911), the chordwise velocity U is taken to be linearly dependent on x, while the normal velocity V depends on y only, as does the spanwise velocity W. Under these assumptions, the base flow takes the form

$$U = xRe^{-1}F'(y), \tag{2.2a}$$

$$V = -Re^{-1}F(y), \tag{2.2b}$$

$$W = W(y), \tag{2.2c}$$

where the prime denotes differentiation with respect to y, and $F(y)$ and $W(y)$ satisfy the ordinary differential equations

$$F''' - (F')^2 + FF'' + 1 = 0, \tag{2.3a}$$

$$FW' + W'' = 0, \tag{2.3b}$$

with the boundary conditions

$$F(0) = F'(0) = W(0) = 0, \tag{2.4a}$$

$$F'(\infty) = 1, \qquad W(\infty) = 1. \tag{2.4b}$$

Swept Hiemenz flow constitutes an exact solution of the steady incompressible Navier–Stokes equations; its general shape and streamlines are sketched in figure 1. For further reference, the thickness of the boundary layer based on the spanwise velocity profile is 3.05 in non-dimensional units. This model is valid only close to the attachment line since the chordwise velocity component becomes unbounded for increasing x. Despite these limitations, the above model is in good agreement with experiments (Gaster 1967; Poll 1979).

In the following analysis, we further assume the perturbations $(\hat{u}, \hat{v}, \hat{w}, \hat{p})$ of the basic flow to display the same chordwise structure, i.e. $\hat{u}$ scales linearly in the chordwise x-direction and $\hat{v}$ and $\hat{w}$ are independent of x. This assumption is commonly referred to as the Görtler (1955)–Hämmerlin (1955) assumption. The total velocity and pressure fields therefore read

$$\begin{pmatrix} u \\ v \\ w \\ p \end{pmatrix} = \begin{pmatrix} xRe^{-1}F'(y) \\ -Re^{-1}F(y) \\ W(y) \\ P(x, y) \end{pmatrix} + \begin{pmatrix} x\hat{u}(y, z, t) \\ \hat{v}(y, z, t) \\ \hat{w}(y, z, t) \\ \hat{p}(x, y, z, t) \end{pmatrix}. \tag{2.5}$$

Translational invariance in the spanwise z-direction allows us to expand perturbations into Fourier series in z. The Fourier coefficients $(\check{u}, \check{v}, \check{w}, \check{p})$ corresponding to a given spanwise wavenumber k satisfy the linear system of perturbation equations

$$\left(\frac{\partial}{\partial t} - F\frac{\partial}{\partial y} - \Delta + \mathrm{i}kReW + 2F'\right)\check{u} + F''\check{v} = 0, \tag{2.6a}$$

$$\left(\frac{\partial}{\partial t} - F\frac{\partial}{\partial y} - \Delta + \mathrm{i}kReW - F'\right)\check{v} + \frac{\partial \check{p}}{\partial y} = 0, \tag{2.6b}$$

$$\left(\frac{\partial}{\partial t} - F\frac{\partial}{\partial y} - \Delta + \mathrm{i}kReW\right)\check{w} + ReW'\check{v} + \mathrm{i}k\check{p} = 0, \tag{2.6c}$$

$$\check{u} + \frac{\partial \check{v}}{\partial y} + \mathrm{i}k\check{w} = 0, \tag{2.6d}$$

with $\Delta = \partial^2/\partial y^2 - k^2$.

Equations (2.6) are referred to as the direct system. The no-slip condition at the wall and the requirement that perturbations vanish for large y imply the following direct boundary conditions:

$$\check{u} = \check{w} = 0 \qquad \text{at} \quad y = 0, \tag{2.7a}$$

$$\check{v} = \check{v}_w(t) \qquad \text{at} \quad y = 0, \tag{2.7b}$$

$$\check{u} = \check{v} = \check{w} = 0 \qquad \text{at} \quad y = \infty, \tag{2.7c}$$

where $\check{v}_w(t)$ stands for the imposed wall-normal blowing/suction velocity in the flow control context. When the optimal perturbation problem is considered, it is understood that $\hat{v}_w(t) = 0$.

Upon eliminating the pressure and spanwise velocity perturbations, the system (2.6) reduces to

$$\mathscr{A}\frac{\partial}{\partial t}\begin{bmatrix}\check{v}\\ \check{u}\end{bmatrix} + \mathscr{B}\begin{bmatrix}\check{v}\\ \check{u}\end{bmatrix} = 0, \tag{2.8}$$

where the y-differential operators $\mathscr{A}$ and $\mathscr{B}$ stand for

$$\mathscr{A} = \begin{bmatrix}\Delta & 0\\ 0 & 1\end{bmatrix}, \tag{2.9a}$$

$$\mathscr{B} = \begin{bmatrix}\left(-F' - F\dfrac{\partial}{\partial y} - \Delta + \mathrm{i}kReW\right)\Delta & -2F'' - 2F'\dfrac{\partial}{\partial y}\\ F''' - F''\dfrac{\partial}{\partial y} - \mathrm{i}kReW'' & \\ F'' & -F\dfrac{\partial}{\partial y} - \Delta + \mathrm{i}kReW + 2F'\end{bmatrix}, \tag{2.9b}$$

with the boundary conditions

$$\check{u} = \frac{\partial \check{v}}{\partial y} = 0 \qquad \text{at} \quad y = 0, \tag{2.10a}$$

$$\check{v} = \check{v}_w(t) \qquad \text{at} \quad y = 0, \tag{2.10b}$$

$$\check{u} = \check{v} = \frac{\partial \check{v}}{\partial y} = 0 \qquad \text{at} \quad y = \infty. \tag{2.10c}$$

The linear stability properties of (2.8)–(2.10) have previously been studied by Hall *et al.* (1984). The possibility of non-modal transient energy growth has been demonstrated in Obrist & Schmid (2003*b*).

In what follows the $\check{}$ sign is omitted and operators $\mathscr{A}$ and $\mathscr{B}$ are replaced by their discretized counterparts $\boldsymbol{A}$ and $\boldsymbol{B}$. The state vector and the applied wall blowing/suction are denoted $q = (v, u)^T$ and $q_w = (v_w, u_w = 0)^T$ respectively.

3. Elements of optimization theory

Two general goals are pursued in this study: first, the initial perturbation that results in a maximum energy growth over a specified time interval $[0, T_p]$ is determined; secondly, the optimal wall blowing and suction sequence applied over a given time interval $[0, T_c]$ is sought so that the energy growth of this initial perturbation is minimized. In general, the time interval T_p may differ from T_c. We use the convention that T, with no subscript, can equally represent T_p or T_c. For the sake of clarity, table 1 summarizes the principal notations.

Quantity	Symbol	Meaning
Energy	$E(t)$	Kinetic energy of the perturbations at time t integrated over a box centred about the attachment-line, $E(t)=\frac{\sqrt{3}}{2}\int_{-\sqrt{3}}^{\sqrt{3}}\int_0^{\infty}\int_0^{1/k}(x^2u^*u+v^*v+w^*w)\,\mathrm{d}x\,\mathrm{d}y\,\mathrm{d}z$ i.e. $E(t)=\int_0^{\infty}(u^*u+v^*v+w^*w)\,\mathrm{d}y$
	E_{max}	Maximum kinetic energy reached by the overall optimal perturbation
	G_{max}	Maximum kinetic energy growth sustainable by a combination of eigenfunctions as computed by Obrist & Schmid (2003*b*)
Time	T_p	Optimization time used to compute finite-time optimal perturbations
	T_c	Optimization time used to compute the optimal control
	T	Optimization time, T_p or T_c, depending on the context
	T_{max}	Time when the energy maximum E_{max} is reached

TABLE 1. Nomenclature for energy and time quantities.

The general approach is fairly straightforward (Gunzburger 1997; Bewley 2001 among others): given the governing linear equations (2.8)–(2.10) and a quantified objective, standard optimization techniques are employed to find the optimal perturbation, or the optimal control wall-normal blowing to suppress the growth of perturbations. Optimization variables – such as, in our case, the initial condition $q(y,0)$ or the blowing/suction time series $q_w(t)$ – are iteratively improved until the stated objective – such as maximum or minimum energy growth over a finite time span – is achieved. Gradient-based optimization techniques (Press *et al.* 1992) have been widely used for this purpose, as they are very efficient and applicable to large-scale systems. In general, gradient-based optimization algorithms require the following three essential components: (i) an objective functional $\mathscr{I}$ that provides a performance measure with respect to the adjustable optimization variables; (ii) an algorithm to compute the gradient of the objective functional with respect to the optimization variables; (iii) a technique to improve the previous set of optimization variables based on the objective functional gradient.

An iterative algorithm based on these three steps leads, when carefully designed, to a locally optimal set of optimization variables. The present section provides the foundations underlying the design of the optimization procedure. Andersson *et al.* (1999) and Corbett & Bottaro (2001*a*) provided a convenient framework which is used as a starting point for the analysis. However, significant extensions and improvements proved to be necessary in order to arrive at a workable formulation, as outlined below.

3.1. *Objective functional and scalar products*

The objective functional represents a measure of how well the objectives of the optimization procedure have been attained. In our case, the functional

$$\mathscr{I}=\frac{E(T)}{E(0)}+\frac{\alpha^2}{2}\frac{1}{T}\int_0^T E(t)\,\mathrm{d}t+\frac{l^2}{2}\langle\!\langle \boldsymbol{q}_w,\boldsymbol{q}_w\rangle\!\rangle \tag{3.1}$$

is used. The scalar product $\langle\langle .\,,\, . \rangle\rangle$ appearing in (3.1) is defined as

$$\langle\langle \boldsymbol{q}_1, \boldsymbol{q}_2 \rangle\rangle = \frac{1}{T} \int_0^T \boldsymbol{q}_1^* \boldsymbol{M}_\diamond \boldsymbol{q}_2 \, \mathrm{d}t + \text{c.c.}, \tag{3.2}$$

where the symbol c.c. denotes the complex conjugate. The scalar product $\langle\langle \boldsymbol{q}_w, \boldsymbol{q}_w \rangle\rangle$ is then a suitably weighted measure of the wall-blowing energy, as discussed below. Similarly, the scalar product

$$[\![\boldsymbol{q}_1, \boldsymbol{q}_2]\!] = \int_0^\infty \boldsymbol{q}_1^* \boldsymbol{M}_\square \boldsymbol{q}_2 \, \mathrm{d}y + \text{c.c.} \tag{3.3}$$

is introduced so that the perturbation kinetic energy at time t defined in table 1 may be expressed as $E(t) = [\![\boldsymbol{q}(y,t), \boldsymbol{q}(y,t)]\!]$, i.e. solely in terms of the velocity components u and v.

The linear differential operators $\boldsymbol{M}_\square$ and $\boldsymbol{M}_\diamond$ appearing in the definitions of the perturbation energy and the wall blowing energy via the scalar products (3.2) and (3.3) arise from the following considerations: by taking advantage of the continuity equation and the boundary conditions (2.10), we find through successive integrations by parts applied to $E(t)$ defined in table 1 that

$$\boldsymbol{M}_\square = -\frac{1}{k^2} \begin{bmatrix} \Delta & \dfrac{\partial}{\partial y} \\ -\dfrac{\partial}{\partial y} & -1 - k^2 \end{bmatrix}. \tag{3.4}$$

The operator $\boldsymbol{M}_\diamond$ appearing in (3.2) is chosen to be

$$\boldsymbol{M}_\diamond = \begin{bmatrix} s_\diamond(t) & 0 \\ 0 & 0 \end{bmatrix}, \tag{3.5}$$

where the switch function $s_\diamond(t)$ is a suitably chosen scalar function. If $s_\diamond$ were set to unity between $t = 0$ and $t = T_c$, the control energy appearing in (3.1) would simply be the kinetic energy $\langle\langle \boldsymbol{q}_w, \boldsymbol{q}_w \rangle\rangle = (1/T_c) \int_0^{T_c} v_w^* v_w \, \mathrm{d}t$ of the wall-normal velocity v_w. However, strong blowing at $t = 0$ or $t = T_c$ results in numerical difficulties. By setting $s_\diamond(t)$ to take very high values at both ends of the control time interval (Corbett & Bottaro 2001*b*), strong blowing or suction at $t = 0$ or T_c is automatically discarded by the optimization algorithm since their weighted blowing energy $\langle\langle \boldsymbol{q}_w, \boldsymbol{q}_w \rangle\rangle$ is too high. In the present computations, a function of the form $s_\diamond(t) = 1/(1 - \exp[-t^2] - \exp[-(T_c - t)^2])$ has been chosen, which is nearly unity for most of the control time interval $[0, T_c]$, but tends to infinity at both endpoints.

As outlined in § 3.2, the optimization procedure requires the introduction of Lagrange multipliers, or so-called adjoint variables $\tilde{\boldsymbol{q}}(y,t)$, $\tilde{\boldsymbol{q}}_0(y)$ and $\tilde{\boldsymbol{q}}_w(t)$, and three additional scalar products

$$(\tilde{\boldsymbol{q}}_1, \tilde{\boldsymbol{q}}_2) = \int_0^T \int_0^\infty \tilde{\boldsymbol{q}}_1^* \tilde{\boldsymbol{q}}_2 \, \mathrm{d}y \, \mathrm{d}t + \text{c.c.}, \tag{3.6a}$$

$$[\tilde{\boldsymbol{q}}_1, \tilde{\boldsymbol{q}}_2] = \int_0^\infty \tilde{\boldsymbol{q}}_1^* \tilde{\boldsymbol{q}}_2 \, \mathrm{d}y + \text{c.c.}, \tag{3.6b}$$

$$\langle \tilde{\boldsymbol{q}}_1, \tilde{\boldsymbol{q}}_2 \rangle = \int_0^T \tilde{\boldsymbol{q}}_1^* \tilde{\boldsymbol{q}}_2 \, \mathrm{d}t + \text{c.c.} \tag{3.6c}$$

A single vector space $\boldsymbol{\Omega} = \boldsymbol{q} \times \boldsymbol{q}_0 \times \boldsymbol{q}_w \times \tilde{\boldsymbol{q}} \times \tilde{\boldsymbol{q}}_0 \times \tilde{\boldsymbol{q}}_w$ including all the direct and adjoint variables may naturally be introduced. A scalar product combining all the previous ones,

$$\{\boldsymbol{Q}^1, \boldsymbol{Q}^2\} = (\boldsymbol{q}^1, \boldsymbol{q}^2) + [[\boldsymbol{q}_0^1, \boldsymbol{q}_0^2]] + \langle\langle \boldsymbol{q}_w^1, \boldsymbol{q}_w^2 \rangle\rangle + (\tilde{\boldsymbol{q}}^1, \tilde{\boldsymbol{q}}^2) + [\tilde{\boldsymbol{q}}_0^1, \tilde{\boldsymbol{q}}_0^2] + \langle \tilde{\boldsymbol{q}}_w^1, \tilde{\boldsymbol{q}}_w^2 \rangle, \quad (3.7)$$

is then conveniently defined for arbitrary elements $\boldsymbol{Q}^i = (\boldsymbol{q}^i, \boldsymbol{q}_0^i, \boldsymbol{q}_w^i, \tilde{\boldsymbol{q}}^i, \tilde{\boldsymbol{q}}_0^i, \tilde{\boldsymbol{q}}_w^i)$ of $\boldsymbol{\Omega}$. In § 3.2 it is demonstrated that the six scalar products (3.2), (3.3), (3.6*a*), (3.6*b*), (3.6*c*) and (3.7) are indeed necessary to correctly formulate the optimization procedure in the reduced $u - v$ setting.

The form of the objective functional (3.1) has been suggested by Corbett & Bottaro (2001*b*), among others. The first term $E(T)/E(0)$ stands for the energy amplification between $t = 0$ and T. In searching for optimal initial perturbations, we try to maximize this term; by contrast, in searching for optimal control strategies, the objective is to minimize it. Note that, as the optimal perturbation is the initial disturbance, the energy of which increases the most between $t = 0$ and T_p, the control parameters α and l are set to zero when computing the optimal perturbation. The objective functional then reduces to the energy amplification term.

The control problem may similarly be regarded as the minimization of the energy ratio $E(T)/E(0)$ for a given initial condition. This procedure does not necessarily yield acceptable results since it does not take into consideration the energy evolution over the full time interval. Substantial energy levels may still be reached between $t = 0$ and $t = T_c$ (Corbett & Bottaro 2001*b*) unless we also include the term $(\alpha^2/2)(1/T)\int_0^T E(t)\,\mathrm{d}t$ which acts as a penalty for excessive transient energy growth within the optimization interval. In what follows the quantity $(1/T)\int_0^T E(t)\,\mathrm{d}t$ is referred to as the mean energy.

It is also important to include the third term $(l^2/2)\langle\langle \boldsymbol{q}_w, \boldsymbol{q}_w \rangle\rangle$ in (3.1), which is a measure of the control cost, in order to avoid excessively strong blowing. The penalty parameter l allows us to set the 'price' of any control effort by weighing the control energy $\langle\langle \boldsymbol{q}_w, \boldsymbol{q}_w \rangle\rangle$ within the objective functional.

The two penalty parameters α and l thus aid in refining and tuning the objective functional by suitably weighing each of its terms.

3.2. *Lagrangian formulation*

To compute the gradient of $\mathscr{I}$ both with respect to the initial condition $\boldsymbol{q}_0$ and the wall-normal blowing sequence $\boldsymbol{q}_w$, a Lagrangian-based approach (Gunzburger 1997) is used. This method has the advantage of not only providing the optimality conditions (Corbett & Bottaro 2001*a*), but also an expression for the gradient of the objective functional $\mathscr{I}$.

Following Andersson *et al.* (1999), Corbett & Bottaro (2001*a*, *b*) and Pralits *et al.* (2002), it is convenient to rewrite the linear system (2.8)–(2.10) governing the reduced state vector $\boldsymbol{q} = (v, u)^T$ in the form

$$\text{reduced system of equations} \qquad F(\boldsymbol{q}) = \frac{\partial}{\partial t}\left(A_i \frac{\partial^i \boldsymbol{q}}{\partial y^i}\right) + B_j \frac{\partial^j \boldsymbol{q}}{\partial y^j} = 0, \quad (3.8a)$$

$$\text{initial conditions} \qquad G(\boldsymbol{q}, \boldsymbol{q}_0) = \boldsymbol{q}(y, 0) - \boldsymbol{q}_0(y) = 0, \quad (3.8b)$$

$$\text{boundary conditions} \qquad H(\boldsymbol{q}, \boldsymbol{q}_w) = \boldsymbol{q}(0, t) - \boldsymbol{q}_w(t) = 0, \quad (3.8c)$$

where the Einstein summation convention has been introduced to yield a compact as well as general form for the partial differential equations. The y-dependent matrices A_i and B_j give the respective weights on each of the derivatives $\partial^i./\partial y^i$

and $\partial^j/\partial y^j$ applied to the variables u, v. In the direct problem (2.8)–(2.10) the sub- and superscripts i and j range from zero to two and from zero to four, respectively. In addition, it is further assumed that the boundary conditions at infinity, as well as the remaining boundary conditions at the wall are satisfied.

The linear system (3.8), can be viewed as a set of equality constraints associated with the optimization problem for the objective functional $\mathscr{I}$. For sufficiently smooth functions F, G, H, the constrained problem can be transformed into an unconstrained one by introducing the Lagrangian

$$\mathscr{L}(\boldsymbol{q}, \boldsymbol{q}_0, \boldsymbol{q}_w, \tilde{\boldsymbol{q}}, \tilde{\boldsymbol{q}}_0, \tilde{\boldsymbol{q}}_w) = \mathscr{I} - (\tilde{\boldsymbol{q}}, F(\boldsymbol{q})) - [\tilde{\boldsymbol{q}}_0, G(\boldsymbol{q}, \boldsymbol{q}_0)] - \langle \tilde{\boldsymbol{q}}_w, H(\boldsymbol{q}, \boldsymbol{q}_w)\rangle. \tag{3.9}$$

The Lagrange multipliers $\tilde{\boldsymbol{q}} = (\tilde{v}, \tilde{u})^T$, $\tilde{\boldsymbol{q}}_0 = (\tilde{v}_0, \tilde{u}_0)^T$, $\tilde{\boldsymbol{q}}_w = (\tilde{v}_w, \tilde{u}_w)^T$ are referred to as the adjoint variables. The Lagrangian (3.9) is defined even when the constraints are not enforced. For this reason, the variables $\boldsymbol{q}$, $\boldsymbol{q}_0$, $\boldsymbol{q}_w$, $\tilde{\boldsymbol{q}}$, $\tilde{\boldsymbol{q}}_0$, $\tilde{\boldsymbol{q}}_w$ can be considered as mutually independent.

The Lagrangian $\mathscr{L}$ is assumed to be differentiable on the vector space $\boldsymbol{\Omega}$ introduced in § 3.1 and may then have stationary points where all its derivatives are equal to zero. We will see next that at these stationary points the system of equations (3.8) is satisfied, and the objective functional $\mathscr{I}$ is stationary. In other words, the solutions of the optimization problem lie at the stationary points of the Lagrangian. At such points the components of the vector $\boldsymbol{Q} = \{\boldsymbol{q}, \boldsymbol{q}_0, \boldsymbol{q}_w, \tilde{\boldsymbol{q}}, \tilde{\boldsymbol{q}}_0, \tilde{\boldsymbol{q}}_w\}$ satisfy the direct and adjoint state equations together with equations referred to as the optimality conditions.

The advantage of the Lagrangian-based formulation is that $\mathscr{L}$ is defined on the entire vector space $\boldsymbol{\Omega}$ whereas $\mathscr{I}$ is defined only on the subdomain $\boldsymbol{\Omega}_c$ of $\boldsymbol{\Omega}$, where the system (3.8) is satisfied. An analytic expression for the gradient of the Lagrangian is available at every point in $\boldsymbol{\Omega}$, from which an analytic expression of the gradient of $\mathscr{I}$ on $\boldsymbol{\Omega}_c$ can be derived. This gradient information is then used to implement the main step in the gradient-based optimization algorithm.

3.3. *Gradient of the objective functional*

The Gateau differential $\mathrm{d}\mathscr{L}$ of the Lagrangian evaluated at point $\boldsymbol{Q}$ is defined as

$$\mathrm{d}\mathscr{L}|_{\boldsymbol{Q}}(\delta \boldsymbol{Q}) = \lim_{\varepsilon \to 0} \frac{\mathscr{L}(\boldsymbol{Q} + \varepsilon \delta \boldsymbol{Q}) - \mathscr{L}(\boldsymbol{Q})}{\varepsilon}. \tag{3.10}$$

Assuming that $\mathscr{L}$ is Fréchet-differentiable, the gradient of the Lagrangian at point $\boldsymbol{Q}$, denoted $\nabla\mathscr{L}(\boldsymbol{Q})$, is such that for any vector $\delta\boldsymbol{Q}$ the following expression holds:

$$\{\nabla\mathscr{L}(\boldsymbol{Q}), \delta \boldsymbol{Q}\} = \mathrm{d}\mathscr{L}|_{\boldsymbol{Q}}(\delta \boldsymbol{Q}), \tag{3.11}$$

with the scalar product introduced in (3.7). The projections of $\nabla\mathscr{L}(\boldsymbol{Q})$ onto the subspaces $\mathtt{span}\{\boldsymbol{q}, 0, 0, 0, 0, 0\}$, $\mathtt{span}\{0, \boldsymbol{q}_0, 0, 0, 0, 0\}$, etc. are denoted by the more convenient symbols $\nabla_{\boldsymbol{q}}\mathscr{L}$, $\nabla_{\boldsymbol{q}_0}\mathscr{L}$, ... and referred to as either ' the $\boldsymbol{q}$, $\boldsymbol{q}_0$, etc. component of the gradient' or 'the gradient with respect to $\boldsymbol{q}$, $\boldsymbol{q}_0$, etc.'

The common procedure in flow control (Gunzburger 1997; Andersson *et al.* 1999; Corbett & Bottaro 2001*a*, *b*; Pralits *et al.* 2002) is to compute, first, the gradients of the Lagrangian with respect to the adjoint variables $\tilde{\boldsymbol{q}}$, $\tilde{\boldsymbol{q}}_0$, $\tilde{\boldsymbol{q}}_w$, and, secondly, the gradient with respect to the flow field $\boldsymbol{q}$. From these calculations, we can recover the direct and adjoint systems, as well as the direct and adjoint boundary conditions. The gradients of the Lagrangian with respect to the control variables $\boldsymbol{q}_0$ and $\boldsymbol{q}_w$, i.e. the initial perturbation and the wall blowing/suction velocity, yield analytic expressions for the gradients of the objective functional with respect to $\boldsymbol{q}_0$ and $\boldsymbol{q}_w$.

Differentiating (3.9) with respect to the adjoint variables yields

$$(\nabla_{\tilde{\boldsymbol{q}}}\mathscr{L}(\boldsymbol{Q}), \delta\tilde{\boldsymbol{q}}) = -(\delta\tilde{\boldsymbol{q}}, F(\boldsymbol{q})), \tag{3.12a}$$

$$[\nabla_{\tilde{\boldsymbol{q}}_0}\mathscr{L}(\boldsymbol{Q}), \delta\tilde{\boldsymbol{q}}_0] = -[\delta\tilde{\boldsymbol{q}}_0, G(\boldsymbol{q}, \boldsymbol{q}_0)], \tag{3.12b}$$

$$\langle\nabla_{\tilde{\boldsymbol{q}}_w}\mathscr{L}(\boldsymbol{Q}), \delta\tilde{\boldsymbol{q}}_w\rangle = -\langle\delta\tilde{\boldsymbol{q}}_w, H(\boldsymbol{q}, \boldsymbol{q}_w)\rangle. \tag{3.12c}$$

At the stationary points of the Lagrangian $\mathscr{L}$, all three gradients are by definition equal to zero. As the variational terms $\delta\tilde{\boldsymbol{q}}$, $\delta\tilde{\boldsymbol{q}}_0$, $\delta\tilde{\boldsymbol{q}}_w$ may be chosen arbitrarily, F, G and H necessarily have to vanish, thus satisfying the direct system of equations (3.8).

Differentiating (3.9) with respect to the control $\boldsymbol{q}_w$ yields

$$\langle\!\langle\nabla_{\boldsymbol{q}_w}\mathscr{L}(\boldsymbol{Q}), \delta\boldsymbol{q}_w\rangle\!\rangle = l^2\langle\!\langle\boldsymbol{q}_w, \delta\boldsymbol{q}_w\rangle\!\rangle + \langle\tilde{\boldsymbol{q}}_w, \delta\boldsymbol{q}_w\rangle. \tag{3.13}$$

Bearing in mind the definitions (3.2) and (3.6*c*) of the scalar products $\langle\!\langle ., .\rangle\!\rangle$ and $\langle ., .\rangle$, we may write

$$\langle\tilde{\boldsymbol{q}}_w, \delta\boldsymbol{q}_w\rangle = \langle\!\langle\tilde{\boldsymbol{q}}_w, \boldsymbol{M}_\diamond^{-1}\delta\boldsymbol{q}_w\rangle\!\rangle = \langle\!\langle\boldsymbol{M}_\diamond^{-1}\tilde{\boldsymbol{q}}_w, \delta\boldsymbol{q}_w\rangle\!\rangle, \tag{3.14}$$

where $\boldsymbol{M}_\diamond^{-1}$ denotes the matrix $\left[\begin{smallmatrix}(1/s_\diamond) & 0\\ 0 & 0\end{smallmatrix}\right]$. Equation (3.13) may then be rewritten as

$$\langle\!\langle\nabla_{\boldsymbol{q}_w}\mathscr{L}(\boldsymbol{Q}), \delta\boldsymbol{q}_w\rangle\!\rangle = l^2\langle\!\langle\boldsymbol{q}_w, \delta\boldsymbol{q}_w\rangle\!\rangle + \langle\!\langle\boldsymbol{M}_\diamond^{-1}\tilde{\boldsymbol{q}}_w, \delta\boldsymbol{q}_w\rangle\!\rangle. \tag{3.15}$$

This expression has to hold true for any $\delta\boldsymbol{q}_w$ which entails

$$\nabla_{\boldsymbol{q}_w}\mathscr{L}(\boldsymbol{Q}) = l^2\boldsymbol{q}_w + \boldsymbol{M}_\diamond^{-1}\tilde{\boldsymbol{q}}_w. \tag{3.16}$$

At the stationary points of $\mathscr{L}$, the gradient $\nabla_{\boldsymbol{q}_w}\mathscr{L}$ vanishes, thereby yielding the first optimality condition

$$l^2\boldsymbol{q}_w + \boldsymbol{M}_\diamond^{-1}\tilde{\boldsymbol{q}}_w = 0. \tag{3.17}$$

Differentiation of (3.9) with respect to the initial perturbation $\boldsymbol{q}_0$ leads to

$$[\![\nabla_{\boldsymbol{q}_0}\mathscr{L}(\boldsymbol{Q}), \delta\boldsymbol{q}_0]\!] = -2\frac{E(T)}{E(0)^2}[\![\boldsymbol{q}_0, \delta\boldsymbol{q}_0]\!] + [\tilde{\boldsymbol{q}}_0, \delta\boldsymbol{q}_0], \tag{3.18}$$

which, according to definitions (3.3) and (3.6*b*), is equivalent to

$$[\![\nabla_{\boldsymbol{q}_0}\mathscr{L}(\boldsymbol{Q}), \delta\boldsymbol{q}_0]\!] = -2\frac{E(T)}{E(0)^2}[\![\boldsymbol{q}_0, \delta\boldsymbol{q}_0]\!] + [\![\boldsymbol{M}_\square^{-1}\tilde{\boldsymbol{q}}_0, \delta\boldsymbol{q}_0]\!], \tag{3.19}$$

where $\boldsymbol{M}_\square^{-1}$ is the inverse of the matrix differential operator $\boldsymbol{M}_\square$. The gradient of the Lagrangian with respect to the initial perturbation is then

$$\nabla_{\boldsymbol{q}_0}\mathscr{L}(\boldsymbol{Q}) = -2\frac{E(T)}{E(0)^2}\boldsymbol{q}_0 + \boldsymbol{M}_\square^{-1}\tilde{\boldsymbol{q}}_0, \tag{3.20}$$

and the second optimality condition readily follows:

$$-2\frac{E(T)}{E(0)^2}\boldsymbol{q}_0 + \boldsymbol{M}_\square^{-1}\tilde{\boldsymbol{q}}_0 = 0. \tag{3.21}$$

It remains to calculate the derivative of $\mathscr{L}$ with respect to the direct state variable $\boldsymbol{q}$. The procedure is straightforward, but algebraically involved. Only the final result is given here. At the stationary points of the Lagrangian $\mathscr{L}$, the gradient $\nabla_{\boldsymbol{q}}\mathscr{L}$ vanishes and the adjoint variables are found, through successive integrations by parts, to satisfy

$$(-1)^{i+1}\frac{\partial^{i+1}(A_i^*\tilde{\boldsymbol{q}})}{\partial y^i\partial t} + (-1)^j\frac{\partial^j(B_j^*\tilde{\boldsymbol{q}})}{\partial y^j} - \alpha^2\boldsymbol{M}_\square^{-1}\boldsymbol{q} = 0, \tag{3.22}$$

with the adjoint boundary conditions

$$\tilde{v} = \tilde{u} = \frac{\partial \tilde{v}}{\partial y} = 0 \qquad \text{at} \quad y = 0, \infty, \tag{3.23}$$

and the adjoint terminal condition

$$(-1)^i \frac{\partial^i (A_i^* \tilde{\boldsymbol{q}})}{\partial y^i}(T) = \frac{2}{E(0)} \boldsymbol{M}_{\square} \boldsymbol{q}(T). \tag{3.24}$$

The * superscript applied to a matrix stands for its conjugate transpose. The adjoint system (3.22), (3.23) is similar to the direct system, but it is only well-posed if it is integrated backward in time. For a non-zero parameter α, a forcing term involving the direct state vector $\boldsymbol{q}$ appears in equation (3.22).

The above integrations by parts further yield the following expressions for $\tilde{\boldsymbol{q}}_w$ and $\tilde{\boldsymbol{q}}_0$ in terms of the adjoint variable $\tilde{\boldsymbol{q}}$ evaluated at $y = 0$ and $t = 0$:

$$\tilde{\boldsymbol{q}}_w = (-1)^{j-1} \frac{\partial^{j-1} (B_j^* \tilde{\boldsymbol{q}})}{\partial y^{j-1}}(y = 0) + (-1)^i \frac{\partial^i (A_i^* \tilde{\boldsymbol{q}})}{\partial y^{i-1} \partial t}(y = 0), \tag{3.25a}$$

$$\tilde{\boldsymbol{q}}_0 = (-1)^i \frac{\partial^i (A_i^* \tilde{\boldsymbol{q}})}{\partial y^i}(t = 0). \tag{3.25b}$$

Substitution of (3.25*a*) and (3.25*b*) into (3.16) and (3.20) leads to the final equations for the gradients with respect to the control variable $\boldsymbol{q}_w$ and the initial perturbation $\boldsymbol{q}_0$ in terms of the adjoint field $\tilde{\boldsymbol{q}}$:

$$\nabla_{\boldsymbol{q}_w} \mathscr{L}(\boldsymbol{Q}) = l^2 \boldsymbol{q}_w + \boldsymbol{M}_{\diamond}^{-1} \left((-1)^{j-1} \frac{\partial^{j-1} (B_j^* \tilde{\boldsymbol{q}})}{\partial y^{j-1}}(y=0) + (-1)^i \frac{\partial^i (A_i^* \tilde{\boldsymbol{q}})}{\partial y^{i-1} \partial t}(y=0) \right), \tag{3.26a}$$

$$\nabla_{\boldsymbol{q}_0} \mathscr{L}(\boldsymbol{Q}) = (-1)^i \boldsymbol{M}_{\square}{}^{-1} \frac{\partial^i (A_i^* \tilde{\boldsymbol{q}})}{\partial y^i}(t = 0) - 2 \frac{E(T)}{E(0)^2} \boldsymbol{q}_0. \tag{3.26b}$$

The gradients of the Lagrangian with respect to the initial disturbance and with respect to the wall-normal blowing/suction sequence are therefore given as explicit functions of the direct variables $\boldsymbol{q}$, $\boldsymbol{q}_0$, $\boldsymbol{q}_w$ and the adjoint field $\tilde{\boldsymbol{q}}$ at $t = 0$. In the constrained subspace $\boldsymbol{\Omega}_c$ where equations (3.8*b*, *c*) are satisfied, the gradient of the Lagrangian simply reduces to

$$\nabla_{\boldsymbol{q}_0} \mathscr{L}(\boldsymbol{Q}) = \nabla_{\boldsymbol{q}_0} \mathscr{I}(\boldsymbol{Q}), \tag{3.27a}$$

$$\nabla_{\boldsymbol{q}_w} \mathscr{L}(\boldsymbol{Q}) = \nabla_{\boldsymbol{q}_w} \mathscr{I}(\boldsymbol{Q}). \tag{3.27b}$$

The local shape of the objective functional $\mathscr{I}$ is thus the same as the shape of the Lagrangian $\mathscr{L}$ in the constrained space $\boldsymbol{\Omega}_c$. In particular, at the points of $\boldsymbol{\Omega}_c$ where the objective functional is maximal or minimal, the gradient $\nabla \mathscr{L}$ of the Lagrangian and the gradient $\nabla \mathscr{I}$ of the objective functional are identically zero. The solutions of the optimization problem thus lie at the stationary points of the Lagrangian.

Knowledge of the gradient of the objective functional for any given value of $\boldsymbol{q}_0$ and $\boldsymbol{q}_w$ forms the basis of the numerical optimization algorithm. The local direction of steepest ascent/descent of the objective functional with respect to $\boldsymbol{q}_0$ or $\boldsymbol{q}_w$ is used to iteratively improve upon a guess value $\boldsymbol{q}_0^0$ or $\boldsymbol{q}_w^0$: if the optimal perturbation is sought, we have to explore the constrained space 'uphill' along the direction defined by $\nabla_{\boldsymbol{q}_0} \mathscr{I}$; if an optimal control $\boldsymbol{q}_w$ is sought, the minimum of $\mathscr{I}$ is approached by exploring the constrained space 'downhill' along the direction of steepest descent given by $-\nabla_{\boldsymbol{q}_w} \mathscr{I}$.

1. Start from a guess value $\boldsymbol{q}_w^0(t)$ for the temporal evolution of the blowing/suction velocity.
'No blowing' is an acceptable guess value for the control since it is compatible with the wall-normal velocity boundary condition for the initial perturbation.

2. Solve the direct problem (2.8)–(2.10).
Using standard numerical techniques, the direct problem is solved forward in time from $t=0$ to $t=T_c$ with initial condition $\boldsymbol{q}_0(y)$ and wall boundary condition $\boldsymbol{q}_w^k(t)$ for the $(k+1)$th optimization step.

3. Compute the terminal condition $\tilde{\boldsymbol{q}}^k(T_c)$ for the adjoint field using equation (3.24).
Solving (3.24) requires the integration of an ordinary differential equation subject to the adjoint boundary conditions (3.23).

4. Solve the adjoint problem (3.22)–(3.23).
The adjoint problem has to be solved backward in time from $t=T_c$ to $t=0$ starting with the terminal value $\tilde{\boldsymbol{q}}^k(T_c)$ from step 3.

5. Compute the gradient of the objective functional with respect to the control variable $\boldsymbol{q}_w$ using equation (3.24$\boldsymbol{a}$).
Solving equation (3.26a) is simplified by our choice of the operator $\boldsymbol{M}_\diamond^{-1}$.

6. Compute the direction of descent.
The direction of descent $\nabla_{desc}^k \mathscr{I}$ is based on the gradient of the objective functional computed in step 5. A conjugate gradient method is used to determine the direction of descent.

7. Change $\boldsymbol{q}_w^k(t)$ into $\boldsymbol{q}_w^{k+1}(t)=\boldsymbol{q}_w^k(t)+s^k\nabla_{desc}^k\mathscr{I}$.
The previous estimate $\boldsymbol{q}_w^k(t)$ is improved by stepping in the direction of descent computed in step 6. The amount of correction, given by s^k, is determined by a line search algorithm (Press *et al.* 1992) which computes $s^k>0$ so that $\mathscr{I}(\boldsymbol{q}_w^k(t)+s^k\nabla_{desc}^k\mathscr{I})$ reaches a minimum with respect to s^k.

8. Return to step 2 and iterate until converged.

TABLE 2. Structure of the optimization algorithm for the optimal control problem.

3.4. *Optimization procedure*

The optimal control procedure is detailed here. The algorithm is based on the gradient information given in the previous section. The control is applied only during the time interval $[0, T_c]$ and the goal is to minimize the objective functional (3.1) with $T=T_c$. The gradient-based optimization algorithm to minimize $\mathscr{I}$ improves iteratively the wall-blowing sequence $\boldsymbol{q}_w^k$ at each iteration k, by modifying it along a well-chosen direction of descent $\nabla_{desc}^k\mathscr{I}$.

The simplest choice is to proceed along the gradient of $\mathscr{I}$, by using $\nabla_{desc}^k\mathscr{I}=-\nabla_{\boldsymbol{q}_w}^k\mathscr{I}$; this direction should lead, at least locally, to the strongest decrease in the objective functional. The drawback of such a steepest descent technique is that the information used is only local, even though, after a few iterations, a more global picture of the objective functional emerges. Conjugate gradient techniques, which take into account the directions of descent evaluated in previous steps (Greenbaum 1997), typically increase the convergence rate of the algorithm at a very low additional computational cost; in many cases they are necessary to ensure convergence of the procedure. The optimization algorithm is summarized in table 2.

4. Application to swept Hiemenz flow and numerical implementation

By gathering the results of the previous section, the adjoint system associated to the direct system (2.8)–(2.10) may be written as:

$$\tilde{\boldsymbol{A}}\frac{\partial}{\partial t}\begin{bmatrix}\tilde{v}\\ \tilde{u}\end{bmatrix}+\tilde{\boldsymbol{B}}\begin{bmatrix}\tilde{v}\\ \tilde{u}\end{bmatrix}-\frac{\alpha^2}{2}\boldsymbol{M}_\square^{-1}\begin{bmatrix}v\\ u\end{bmatrix}=0, \tag{4.1}$$

where the adjoint operators $\tilde{\boldsymbol{A}}$ and $\tilde{\boldsymbol{B}}$ are

$$\tilde{\boldsymbol{A}} = \begin{bmatrix} \Delta & 0 \\ 0 & 1 \end{bmatrix}, \tag{4.2a}$$

$$\tilde{\boldsymbol{B}} = \begin{bmatrix} \left(-F\frac{\partial}{\partial y} + \Delta + \mathrm{i}kReW \right)\Delta & -F'' \\ -2F'\frac{\partial^2}{\partial y^2} + 2(\mathrm{i}kReW' - F'')\frac{\partial}{\partial y} & \\ -2F'\frac{\partial}{\partial y} & \left(-F\frac{\partial}{\partial y} + \Delta + \mathrm{i}kReW - 3F' \right) \end{bmatrix}, \tag{4.2b}$$

with adjoint boundary conditions (3.23). According to (3.24), the terminal condition of the adjoint system is related to the terminal value of the direct state vector via

$$\tilde{\boldsymbol{q}}(y, T) = \frac{-1}{E(0)} \boldsymbol{A}^{-1} \boldsymbol{M}_{\square} \boldsymbol{q}(T). \tag{4.3}$$

The operators $\boldsymbol{A}$ and $\boldsymbol{M}_{\square}$ are given in (2.9*a*) and (3.4), respectively. The boundary conditions (3.23) are required to invert the second-order operator $\boldsymbol{A}$, in order to compute $\tilde{\boldsymbol{q}}(y, T)$ from (4.3).

The gradients of the objective functional with respect to the control variable, $\nabla_{\boldsymbol{q}_w} \mathscr{I}$, and with respect to the initial perturbations, $\nabla_{\boldsymbol{q}_0} \mathscr{I}$, defined in (3.27) and given by (3.26) become

$$\nabla_{\boldsymbol{q}_w} \mathscr{I} = l^2 \boldsymbol{q}_w + \boldsymbol{M}_{\diamond}^{-1} \left(\frac{\partial^3}{\partial y^3} - F\frac{\partial^2}{\partial y^2} \right) \tilde{\boldsymbol{q}}(y = 0, t), \tag{4.4a}$$

$$\nabla_{\boldsymbol{q}_0} \mathscr{I} = \boldsymbol{M}_{\square}^{-1} \boldsymbol{A}\, \tilde{\boldsymbol{q}}(y, t = 0) - \frac{E(T)}{E(0)^2} \boldsymbol{q}_0, \tag{4.4b}$$

where the operator $\boldsymbol{M}_{\diamond}$ is given in (3.5). The 'numerical difficulties' alluded to in § 3.1 which resulted in the introduction of the switch function $s_{\diamond}$ now become clear. The initial disturbance $\boldsymbol{q}(t = 0)$ on which control is applied is computed under the assumption of zero wall-normal velocity at the wall. Since no boundary condition at the wall is imposed on the higher derivatives of the adjoint field $\tilde{\boldsymbol{q}}$, the gradient $\nabla^k_{\boldsymbol{q}_w} \mathscr{I}$ may not vanish at $t = 0$. Thus, the wall-blowing sequence $\boldsymbol{q}^k_w$ computed at optimization step k, augmented by a fraction of the gradient $s^k \nabla^k_{\boldsymbol{q}_w} \mathscr{I}$, may not satisfy the homogeneous wall condition at $t = 0$. Similarly, at $t = T_c$ the adjoint terminal condition is computed from the direct terminal condition and its spatial derivatives up to second order. If the wall-normal velocity v_w or its derivatives do not vanish at the end of the temporal control interval, the terminal condition for the adjoint problem may not satisfy the boundary condition $\tilde{v}(y = 0, T_c) = 0$. The scalar switch function $s_{\diamond}(t)$ introduced in § 3.1 allows a smooth introduction and fading of the wall-normal control velocity v_w at both ends of the control time interval. The control effort at $t = 0$ and $t = T_c$ is brought to zero and any mismatch in the boundary conditions is avoided.

Spatial derivatives have been computed by using a pseudospectral method based on Chebyshev polynomials with a rational function mapping that allows a flexible placement of collocation points within the boundary layer and in the free stream. The temporal evolution is accomplished by a second-order backward-differentiation scheme, after time has been rescaled by k.

In step 6 of the optimization scheme (table 2), the Polak–Ribière conjugate gradient algorithm is implemented to compute the direction of descent. This is followed in step 7 by a line search algorithm based on Brent's method for the computation of optimal perturbations as well as optimal control. Press *et al.* (1992) give a detailed description of these computational techniques.

In order to generate grid-independent results, it was sufficient to use 150 collocation points in the wall-normal direction and a time step $\Delta t = 0.1$. In the majority of computations presented here it took fewer than five iterations of the conjugate gradient algorithm to converge to an optimum for both the optimal control and optimal perturbation problems, with the first step often coming to within 5 % of the optimal value of the objective functional.

5. Optimal perturbations

In their study of non-modal effects in swept Hiemenz flow, Obrist & Schmid (2003*b*) present several computations at a Reynolds number $Re = 550$ and a spanwise wavenumber $k = 0.25$. Their approach is based on an eigenfunction expansion of the linear initial-value problem. With these parameter settings, the flow is found to be asymptotically stable, but susceptible to short-term energy growth. Computations have been performed at the same parameter settings, but additional results are also presented at a Reynolds number $Re = 850$ where the flow is linearly unstable. Even higher Reynolds numbers ($Re = 2000$) have also been investigated to probe the physical mechanisms responsible for transient energy amplification, which was found to take place throughout the parameter range under consideration ($100 \leqslant Re \leqslant 2500,\ 0.05 \leqslant k \leqslant 0.45$).

5.1. *Energy amplification*

The optimal perturbation is defined as the initial disturbance exhibiting the largest energy amplification over a given time interval. Minor modifications to the algorithm outlined in table 2 – i.e. setting $\boldsymbol{q}_w = 0$ (no blowing/suction), using $\boldsymbol{q}_0$ as the control variable and $\nabla_{\boldsymbol{q}_0}\mathscr{I}$ as the associated objective functional gradient – yield a fast and efficient algorithm to determine both the maximum energy amplification and the initial condition that produces it.

In figure 2(*a*) the temporal energy evolution of such initial perturbations for the case of a linearly stable (solid line) or unstable (dashed line) basic flow is displayed. In the linearly stable case ($Re = 550$, $k = 0.25$), transient energy growth amounts to 123 times the initial energy before perturbations eventually decay. In the unstable case ($Re = 850$, $k = 0.25$), high energy levels may be reached significantly earlier than would be possible by a purely exponential growth of the unstable eigenmode only. The time required to amplify the initial energy by a factor 220 is only 15 time units which should be compared to the 200 time units required to amplify the energy of the most unstable mode by the same amount.

Figure 2(*b*) illustrates how the optimization time T_p influences the energy evolution of the optimal perturbations. At a Reynolds number $Re = 550$ and spanwise wavenumber $k = 0.25$, the maximum energy amplification can be achieved by setting the optimization time to $T_p = 14.3$ (solid line). The energy at $t = T_p$ is then 123 times the initial energy. Optimal perturbations for shorter optimization times, e.g. $T_p = 5$, are slightly more amplified initially. Their overall amplification, however, is lower than for the case $T_p = 14.3$. Beyond a specific value of the optimization time, the least stable mode (or the most unstable mode in the linearly unstable parameter regime)

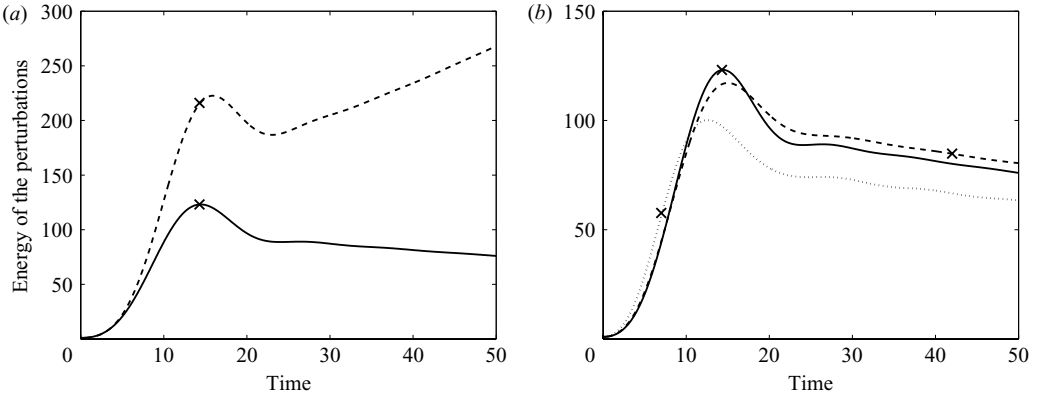

FIGURE 2. (*a*) Disturbance energy E versus time for optimal perturbations in the linearly stable parameter regime ($Re = 550$, $k = 0.25$, solid line), and in the linearly unstable parameter regime ($Re = 850$, $k = 0.25$, dashed line). The optimization time has been set to $T_p = 14.3$ (cross). (*b*) Disturbance energy versus time for the initial perturbations which yield the maximum energy growth at time $T_p = 5$ (dotted line), $T_p = 14.3$ (solid line), and $T_p = 42$ (dashed line). The respective optimization times are indicated by a cross. The parameters have been chosen as $Re = 550$, $k = 0.25$.

prevails. Any optimization time larger than $T_p = 25$ results in a very similar optimal initial condition – the one that excites the least stable mode most efficiently during the early stages of the energy amplification.

Large-time optimal perturbations reach nearly the same maximum amplification, at nearly the same time, as that found for $T_p = 14.3$. Several computations performed at Reynolds numbers ranging from $Re = 500$ to $Re = 2000$ and spanwise wavenumbers, ranging from $k = 0.05$ to $k = 0.4$ have confirmed this property. The initial condition yielding the maximum energy at large times can be identified as the adjoint of the least stable mode (Hill 1995). The overall optimal perturbation thus differs only insignificantly from the adjoint of the least stable mode.

5.2. *Parameter study*

The initial disturbance leading to the maximum energy amplification E_{max}, regardless of the time T_{max} when it is reached, has been computed for several Reynolds numbers and spanwise wavenumbers. In practice, this overall optimal perturbation has been obtained by bracketing the time T_{max} when the maximum energy amplification is reached for different T_p. Figure 3(*a*) displays isocontours of the maximum energy achieved by overall optimal perturbations; the corresponding time T_{max} is shown in figure 3(*b*). In both figures, the thick solid line represents the neutral stability curve for swept Hiemenz flow. At low Reynolds numbers or spanwise wavenumbers, the optimal perturbation could not be determined satisfactorily because of numerical difficulties in evaluating the gradient of the objective function. No gain curves could therefore be obtained in the range $kRe \lesssim 100$. The blank area inside the neutral stability curve identifies the parameter regime where the energy of the optimal perturbation grows monotonically and thus does not exhibit a transient maximum.

We observe that the energy amplification increases with Reynolds number, but decreases when the spanwise wavenumber is increased. The time at which the maximum amplification is reached increases both with Reynolds number and spanwise wavenumber. Energy amplifications ranging from 50 times (for $Re \approx 300$, $0.2 \lesssim k \lesssim 0.4$) up to 1500 times the initial energy (for $Re \approx 2500$, $k \approx 0.1$) have been obtained.

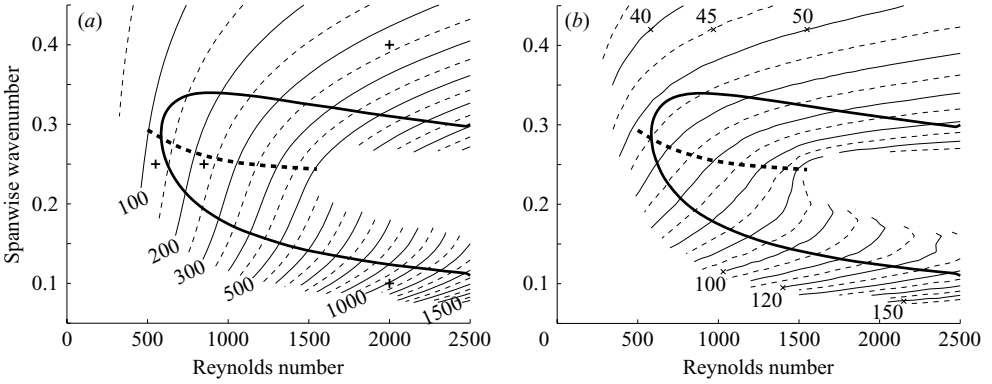

FIGURE 3. (*a*) Isocontours of the maximum energy amplification E_{max} achieved by optimal perturbations (thin lines) in the (Re, k)-plane. The + signs denote the parameter values $(Re, k) = (550, 0.25)$, $(850, 0.25)$, $(2000, 0.1)$ and $(2000, 0.4)$ where most of the calculations have been performed. (*b*) Isocontours of the time T_{max}/k when the maximum energy is reached by optimal perturbations (thin lines) in the (Re, k)-plane. In both figures, the thick solid line represents the neutral stability boundary, and the thick dashed curve is the dividing line separating the two amplification mechanisms discussed in § 5.

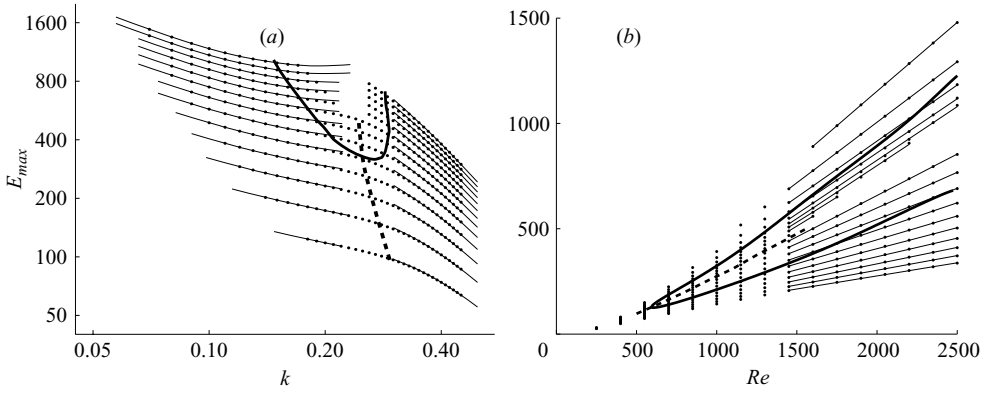

FIGURE 4. (*a*) Maximum energy amplification E_{max} of optimal perturbations versus k for Reynolds numbers ranging from $Re = 500$ (lowest curve) to $Re = 2450$ (highest curve). The scale is logarithmic on both axes. The maximum energy amplification E_{max} decreases slowly with k at small spanwise wavenumbers and strongly with k at high wavenumbers. To guide the eye, least-squares curve fits are displayed by thin solid lines: the data follow a cubic and a quadratic fit at low and high wavenumbers, respectively. The thick dashed line located at $k \sim 0.25$ delineates the two scaling behaviours and the thick solid line represents the neutral stability boundary. (*b*) Maximum energy amplification E_{max} of optimal perturbations versus Reynolds number for spanwise wavenumbers ranging from $k = 0.08$ (highest curve) to $k = 0.44$ (lowest curve). The maximum energy amplification E_{max} increases linearly with the Reynolds number above $Re = 1000$ (thin solid lines). The low and high-k behaviours are delimited by the thick dashed line, and the thick solid line represents the neutral stability boundary.

At low Reynolds numbers, the energy amplification is nearly independent of the spanwise wavenumber; as the Reynolds number increases, however, low-wavenumber perturbations clearly outperform higher-wavenumber disturbances.

At Reynolds numbers higher than 500, two distinct behaviours of the maximum energy amplification with respect to the spanwise wavenumber may be distinguished, as illustrated in figure 4(*a*). At small spanwise wavenumbers the maximum energy

amplification decreases slowly with spanwise wavenumber k while at higher spanwise wavenumbers the maximum energy amplification decreases strongly. The data closely match cubic (at low spanwise wavenumber k) and quadratic (at high k) fitting curves indicated by thin solid lines. Along the thick dashed line at $k \sim 0.25$ both fits are equally close to the data, which reveals a change in the flow behaviour as one proceeds from low to high wavenumbers. In both cases, the maximum energy amplification exhibits a linear dependence with respect to the Reynolds number as shown in figure 4(b).

The thick dashed line in figure 4(a) has been represented in figures 4(b) and 3(a, b) to delineate the high- and low-k parameter regimes. Two distinct physical mechanisms responsible for the energy amplification are suspected to entail the different scalings with the spanwise wavenumber, as further investigated in § 5.4.

Comparison with results from eigenfunction expansions

A similar parameter study based on an eigenfunction expansion analysis has been performed by Obrist & Schmid (2003*b*) in their figure 3. The maximum energy growth obtained by linear combinations of eigenfunctions from the discrete spectrum, denoted G_{max} to distinguish it from E_{max}, is then shown to range from 0 to about 100 as the Reynolds number and spanwise wavenumber vary from 0 to 2500 and from 0.05 to 0.45, respectively. The energy growth G_{max} is found to increase strongly with Reynolds number, but shows little dependence on the spanwise wavenumber at small Reynolds numbers. At higher Reynolds numbers, G_{max} decreases as k tends to 0 or 0.45 with its maximum located inside the neutral curve.

The parameter study by Obrist & Schmid (2003*b*) has the disadvantage of neglecting the continuous part of the spectrum which has a strong quantitative effect on transient growth in swept Hiemenz flow. It is thus not surprising that the energy growth G_{max} computed by an expansion in discrete eigenmodes is up to two orders of magnitude lower than the maximum energy E_{max} calculated by using the present adjoint method. There is also disagreement as to the behaviour of E_{max} at high Reynolds numbers and low spanwise wavenumbers.

Obrist & Schmid (2003*a*) show that the discrete part of the spectrum consists of three branches, two of which have eigenmodes with a strong wall-normal velocity component. Eigenmodes from the continuous spectrum show no specific prevalence of any velocity component. The computation of the optimal purely wall-normal velocity perturbation might thus give an insight into the role of the v-dominant branches of the discrete spectrum in the transient growth process. To this end, the [.,.] scalar product has to be redefined as

$$[\boldsymbol{q}_1, \boldsymbol{q}_2] = \int_0^\infty \boldsymbol{v}_1^* \cdot \boldsymbol{v}_2 \, \mathrm{d}y + \text{c.c.}, \tag{5.1}$$

and a purely wall-normal initial guess $\boldsymbol{q}_0^0 = (\boldsymbol{v}_0^0, 0)^T$ has to be used.

The resulting optimal perturbations then display energy amplifications in agreement with Obrist & Schmid (2003*b*), ranging from less than 1 at low Reynolds numbers to around 10^2 at $Re = 2500$. The spanwise-wavenumber dependence is also recovered, displaying little influence of the wavenumber at low Reynolds numbers; moreover, E_{max} decreases as k tends to 0 or 0.45.

The purely chordwise optimal velocity perturbation has also been computed, but no transient growth could be found. A comparison of these results and the observations of Obrist & Schmid (2003*b*) suggests that (i) the eigenmodes of the two v-dominant branches of the discrete spectrum are the only modes responsible for transient growth,

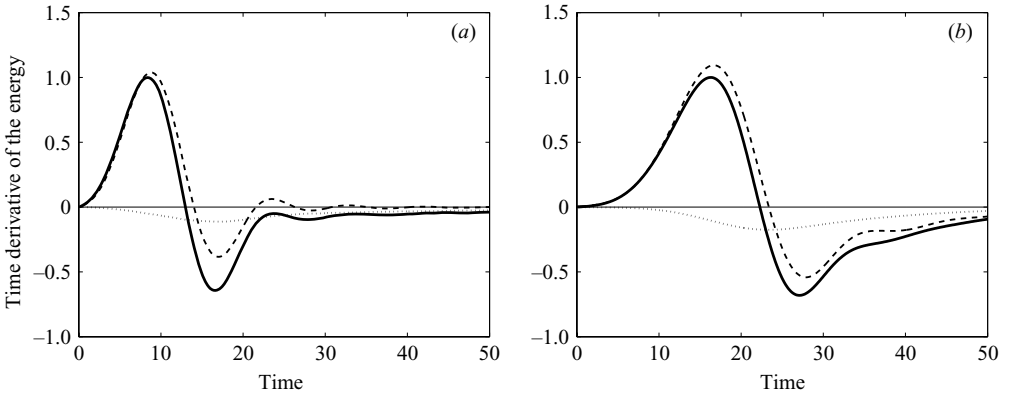

FIGURE 5. Temporal evolution of the dominant terms in the energy equation (5.3) for optimal perturbations, integrated over the (y, z)-plane and normalized with respect to the maximum time derivative of the energy. The production term $-ReW'wv$ (dashed line) is responsible for most of the energy amplification (solid line). The dissipation term $w\Delta w$ is displayed as a dotted line. Parameter settings are (a) $Re = 2000, k = 0.1, T_p = 12.9$ and (b) $Re = 2000, k = 0.4, T_p = 22.2$.

(ii) the u-dominant continuous modes play a merely catalytic role in transient energy growth with a more pronounced efficiency at high Re and low k.

5.3. *Energy transfer analysis*

It is both instructive and straightforward to analyse the flow of energy between various perturbation components in the transient energy growth process. New insight into the dominant terms may lead to a model of the physical mechanism responsible for the observed perturbation dynamics.

By multiplying each of the disturbance equations (2.6*a*)–(2.6*c*) by the appropriate velocity component and subsequently adding the three equations, we obtain a temporal evolution equation for the local kinetic energy density $e = u^2 + v^2 + w^2$ of the perturbation, namely,

$$\frac{\partial e}{\partial t} = Fu\frac{\partial u}{\partial y} + u\Delta u - ReWu\frac{\partial u}{\partial z} - 2F'u^2 - F''uv + Fv\frac{\partial v}{\partial y} + v\Delta v - ReWv\frac{\partial v}{\partial z} + F'v^2 - v\frac{\partial p}{\partial y} + Fw\frac{\partial w}{\partial y} + w\Delta w - ReWw\frac{\partial w}{\partial z} - ReW'wv - w\frac{\partial p}{\partial z}. \quad (5.2)$$

During the transient energy growth phase, terms involving the chordwise velocity component u as well as all pressure gradient terms are found to be negligible compared to the remaining components. The above energy balance may thus be reduced to an equation involving only eight essential terms on the right-hand side:

$$\frac{\partial e}{\partial t} \approx Fv\frac{\partial v}{\partial y} + v\Delta v - ReWv\frac{\partial v}{\partial z} + F'v^2 + Fw\frac{\partial w}{\partial y} + w\Delta w - ReWw\frac{\partial w}{\partial z} - ReW'wv. \quad (5.3)$$

Integrating each term of equation (5.3) separately over the computational (y, z)-domain reveals that the production term $(-ReW'wv)$ clearly dominates at small times (figure 5). At large times, the linear stability property of the flow determines the

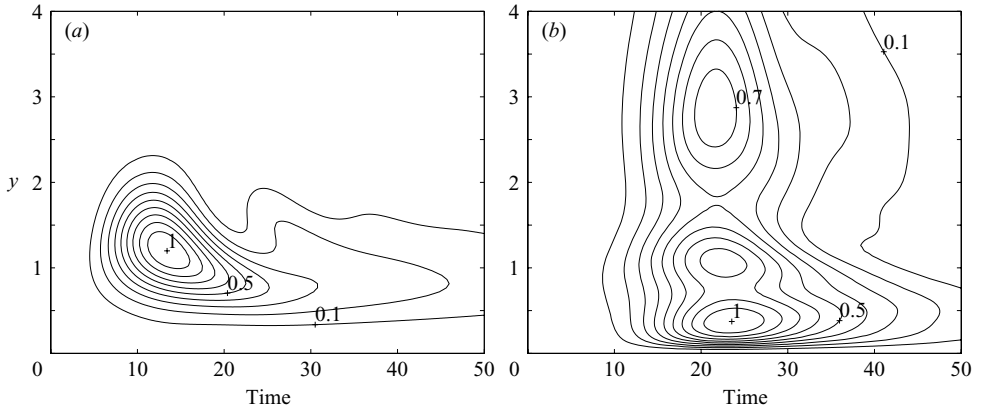

FIGURE 6. Isocontours of $\int_{2\pi/k}(\partial e/\partial t)\,\mathrm{d}z$ (normalized with respect to its maximum) in the (t, y)-plane for optimal perturbations. At low wavenumbers (a), energy production is localized and occurs at a distance of about one-third of the boundary-layer thickness from the wall. At high wavenumbers (b), energy production occurs over a wider area and farther away from the wall. Parameter settings are (a) $Re = 2000$, $k = 0.1$, $T_p = 12.9$ and (b) $Re = 2000$, $k = 0.4$, $T_p = 22.2$.

dominant term in equation (5.3). For linearly stable configurations, the viscous term $w\Delta w$ dominates, thus damping the perturbations. For linearly unstable configurations, the viscous term $w\Delta w$ remains below the production term $(-ReW'wv)$, and, as a consequence, perturbations grow exponentially. Since the dominant production term during the early stage has been identified as $(-ReW'wv)$, the mechanism responsible for transient growth is suspected to be inviscid and two-dimensional in the (y, z)-plane.

The contour plot of $\int_{2\pi/k}(\partial e/\partial t)\,\mathrm{d}z$ in the (t, y)-plane (figure 6*a*) indicates that at low wavenumbers (the case $k = 0.1$ is displayed), energy is amplified in an area located at roughly one-third of the boundary-layer thickness from the wall. The strongest energy amplification rate (contour level labelled 1) occurs at $t = 13.9$, that is, shortly after the perturbation has reached its maximum energy growth ($T_{max} = 13.6$ for $Re = 2000$, $k = 0.1$). At high wavenumbers, disturbance energy production is less localized (figure 6*b*); it is also less intense. Two local maxima appear, one close to the wall ($y \approx 0.5$) and a weaker one located at the outer edge of the boundary layer ($y \approx 3$). Again, the most intense energy amplification rate is found at $t = 25.6$, that is, shortly after the perturbation has reached its maximum energy growth ($T_{max} = 25.5$). In contrast to the low-wavenumber case, where the entire energy amplification mechanism is confined inside the boundary layer, a significant amount of energy is produced in the outer flow.

5.4. *Physical mechanisms leading to transient energy growth*

Both the k-dependence of the maximum energy amplification displayed in figure 4 and the location of maximum energy transfer from the basic flow to the perturbation at low or high wavenumbers, imply the existence of two distinct physical mechanisms at work.

Solutions of the linear initial-value problem provide further support for this proposition. Figures 7 and 8 show the temporal evolution of optimal perturbations at $Re = 2000$ for a representative low ($k = 0.1$) and high ($k = 0.4$) spanwise wavenumber, respectively. Snapshots of the chordwise vorticity and spanwise velocity fields in the $(x = 0)$-plane have been displayed at $t = 0$, $T_{max}/3$, $2T_{max}/3$, T_{max}, $4T_{max}/3$ (from top to

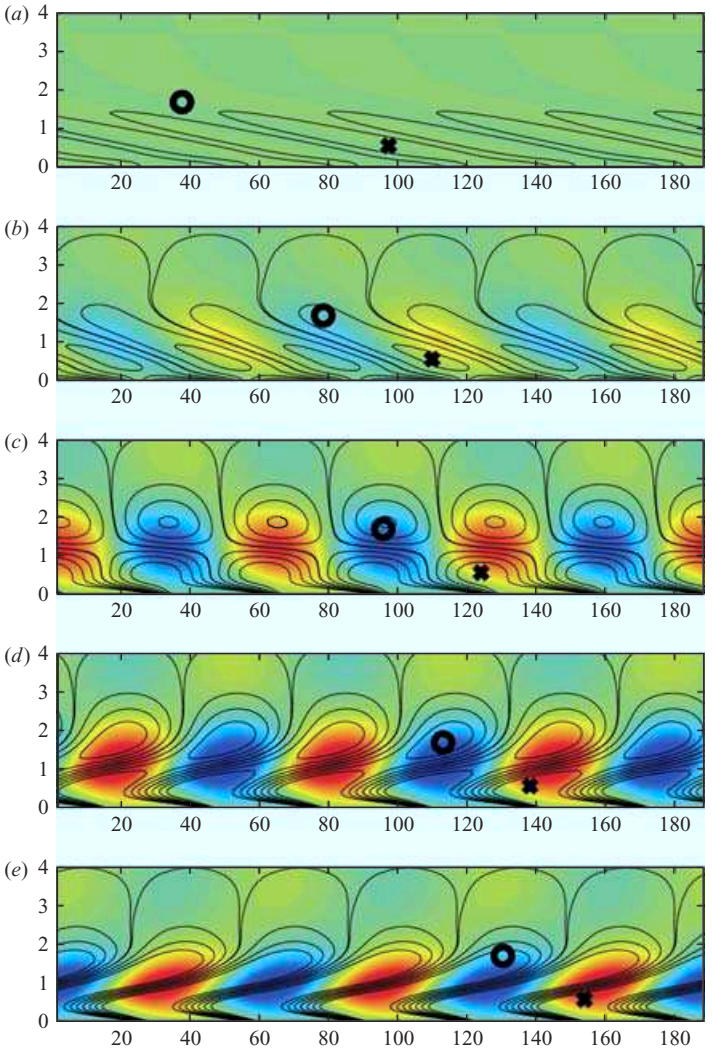

FIGURE 7. Time evolution of the overall optimal perturbation displayed in snapshots of the perturbation field in the (z, y)-plane over three spanwise wavelengths at (a) $t = 0$, (b) $T_{max}/3$, (c) $2T_{max}/3$, (d) T_{max}, (e) $4T_{max}/3$. The sweep W is from left to right. Isocontours of the chordwise vorticity are displayed in solid (positive vorticity) and dashed lines (negative vorticity). The spanwise velocity amplitude w of the disturbance is displayed in colour (red: positive, blue: negative). Symbols have been added to aid the reader in tracking the features of the evolving vortices. The time of maximum energy is $T_{max} = 12.9$ and the parameters have been set to $Re = 2000$, $k = 0.1$, $T_p = 12.9$.

bottom). The colour scheme and contour scales are the same in both figures and for all snapshots, thus aiding in the quantitative comparison between the low and high spanwise wavenumber regimes. For any Reynolds number and spanwise wavenumber, the optimal perturbation resembles a distribution of elongated chordwise vorticity patches inclined against the sweep z-direction as displayed in figures 7(a) and 8(a). The vorticity patches are advected by the sweep velocity W and propagate from left to right between two consecutive snapshots. Under the influence of the basic shear

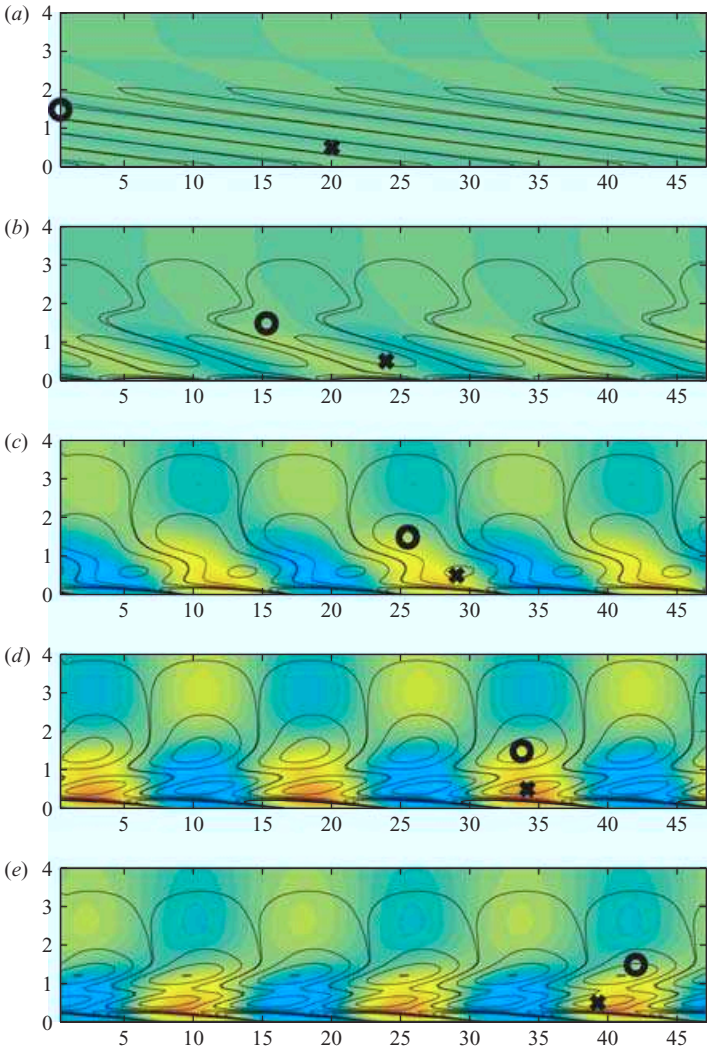

FIGURE 8. Same as in figure 7 for $Re = 2000$, $k = 0.4$ and $T_p = 22.2$; the contour levels and the colour map are the same. The time of maximum energy is $T_{max} = 22.2$.

they tilt up in a manner reminiscent of the Orr mechanism (figures 7*a*, *b* and 8*a*, *b*): the vorticity distribution initially inclined against the shear is compressed, thereby inducing transient energy growth (Haynes 1987; Vanneste 1999).

In the case of low spanwise wavenumber $k = 0.1$ (figure 7), the chordwise vortices are distorted until rectangular vortical cells appear (figure 7*c*). As the 'heads' of the chordwise vortices of one sign pass above the 'feet' of the vortices of the opposite sign, a two-layered array of counter-rotating vortices forms (figure 7*c*). This dipole structure is aligned parallel to the wall at a distance of roughly one-third of the boundary-layer thickness. This region is therefore characterized by strong spanwise velocity excesses and deficits; for example, as the upper-layer vortex of a specific dipole rotates counterclockwise (displayed by solid vorticity contours in figure 7), the centre of the dipole produces a region of strong spanwise excess velocity (displayed in

red). The dipole structure forms at the time when $\int_{1/k}(\partial e/\partial t)\,\mathrm{d}z$ reaches a maximum (figure 5*a*) and it is located at the wall distance where the disturbance energy density is amplified the most according to figure 6(*a*).

Two mechanisms of transient growth are therefore operating at low spanwise wavenumbers: the Orr mechanism via the tilting of the initial vorticity distribution by the basic shear on the one hand and vortex dipole-induced spanwise velocities on the other, the latter being dominant. In the final stage, the rectangular cells split and rearrange – with the 'head' of each vortex merging with the 'foot' of the neighbouring upstream vortex of equal orientation. This event, which is incidental to the transient growth process, occurs at approximately $t = 2T_{max}/3$ (figures 7*c*, *d*).

The evolution of chordwise vortices at higher spanwise wavenumbers displays a different scenario. Most significantly, even if the vortices are still heavily distorted, rectangular vortical dipoles are no longer prominent (figure 8). The vorticity distribution initially inclined against the shear is still tilted by the spanwise shear and the energy amplification arises mainly from the Orr mechanism, as illustrated by the symbols indicating the relative position of the 'head' and 'foot' of the evolving vortex in figure 8. The vortex 'head' overtakes its 'foot', and the disturbance energy reaches a maximum when the vortex is the most compressed, that is, when the 'head' is exactly above the 'foot' (figure 8*d*). In the later stages, vortex splitting never occurs. To provide additional support for the above scenario, computations were performed at even higher spanwise wavenumbers ($k \geqslant 0.8$). The Orr-mechanism has been found to be dominant over vortex dipole-induced spanwise velocities in all high-wavenumber cases.

Examination of the temporal evolution of disturbances in the linearly unstable region, within the neutral stability boundary of figure 3(*a*), reveals the presence of the same physical mechanisms at low and high spanwise wavenumbers, respectively.

6. Optimal control

Within the scope of this study, control is applied via wall-normal blowing and suction given by the normal velocity $v_w(t)$. The influence of the control time T_c on the energy growth of controlled perturbations is investigated and a parameter study in the (α, l)-plane is conducted in order to find the best setting for the control parameters. A physical interpretation of the control mechanisms follows, with particular emphasis on similarities between optimal and constant-gain feedback control.

6.1. *Control of optimal perturbations*

In this section, the Reynolds number is set to either $Re = 550$ or $Re = 850$ with a fixed spanwise wavenumber $k = 0.25$ in order to address the control of linearly stable or unstable flows. For all computations, the initial state is taken as the optimal perturbation for $T_p = 14.3$, and wall-blowing or -suction is applied between $t = 0$ and $t = T_c$.

To investigate the influence of the control time T_c, the control parameters in the objective functional (3.1) have been set to $\alpha = 0.5$, $l = 1$. As will be shown later, such moderate values of α and l lead to satisfactory control strategies.

The control efficiency depends strongly on the control time T_c. The natural choice is to set T_c close to the time at which the uncontrolled optimal perturbation reaches an energy maximum. For a spanwise wavenumber $k = 0.25$ and a Reynolds number $Re = 550$ (figure 9*a*), it amounts to setting $T_c = 14.3$ (diamond). In this case, the optimal wall-normal blowing and suction sequence decreases the energy maximum

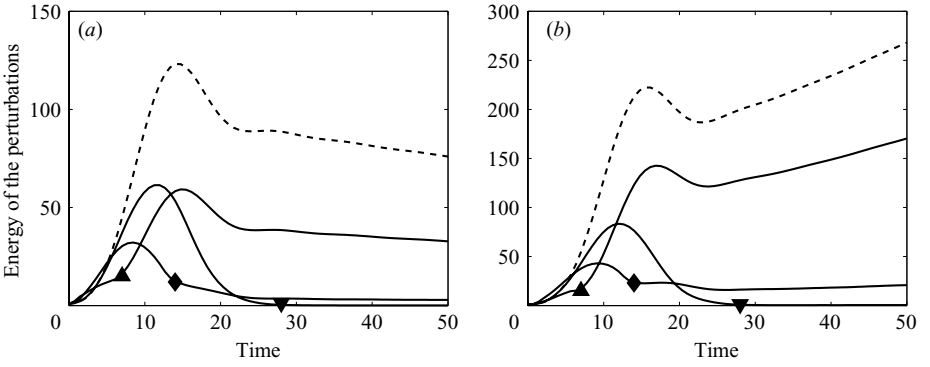

FIGURE 9. Disturbance energy E as a function of time for (a) linearly stable or (b) unstable flow. The dashed line shows the uncontrolled optimal perturbation computed with $T_p = 14.3$. The solid lines display the energy of the same perturbation when control is applied from $t = 0$ to ▲, $T_c = 7$; ◆, $T_c = 14.3$; ▼, $T_c = 28$. The remaining parameters have been set to (a) $Re = 550$ and (b) $Re = 850$, $k = 0.25$, $\alpha = 0.5$, $l = 1$.

to 75 % of its initial value, while the energy at time T_c is decreased by one order of magnitude from $E(T_c)/E(0) = 123$ to $E(T_c)/E(0) = 12$.

For lower values of T_c, the control is less effective in decreasing the energy amplification since the energy transiently increases shortly after the wall-blowing has terminated. For higher values of T_c the energy amplification can be suppressed even further. For example, by choosing $T_c = 28$, i.e. about twice the time at which the energy maximum is reached, the energy decreases to 0.5 times its initial value between $t = 0$ and $t = T_c$. In this case, however, the energy transiently reaches half the level reached by the uncontrolled optimal perturbation between $t = 0$ and T_c.

Similar conclusions hold in the linearly unstable case at $Re = 850$, $k = 0.25$ shown in figure 9(b). Only the case $Re = 550$, $k = 0.25$ will be discussed in the following study of the influence of the control parameters.

The objective functional (3.1) penalizes both transient energy amplification between $t = 0$ and T_c via the α weighting parameter and excessive wall-blowing via the l weighting parameter. Figure 10 reveals the dependence of the objective functional $\mathscr{I}$ (figure 10a), the energy amplification $E(T_c)/E(0)$ (figure 10b), the mean energy $(1/T_c)\int_0^{T_c} E(t)\,\mathrm{d}t$ (figure 10c) and the control energy $\langle\langle \boldsymbol{q}_w, \boldsymbol{q}_w \rangle\rangle$ (figure 10d) on the weighting parameters α and l. Note that the view angle may be different for different subfigures to ensure the best perspective on the surface plot.

When both α and l are low, the mean perturbation energy grows by a few orders of magnitude between $t = 0$ and T_c (figure 10c) owing to a very strong input of control energy (figure 10d). The lowest energy amplification is indeed achieved at these parameter settings (figure 10b) where wall-blowing can be arbitrarily strong because of the low penalty applied to the control effort, but the very large transient energy peak (figure 10c) precludes such control strategies for practical applications.

By assigning a moderate cost, either to the mean energy amplification (by setting α between 0.3 and 1) or to the control energy (by setting l between 0.1 and 2), the mean energy and the spent control energy are dramatically lowered (figure 10c, d) with only a small increase in the energy amplification (hardly noticeable in figure 10b). Such moderate values for α and l are located near the 'shoulder' of the objective function in figure 10(a), where the thick solid line ($\alpha = 0.5$) crosses the thick dashed line ($l = 1$).

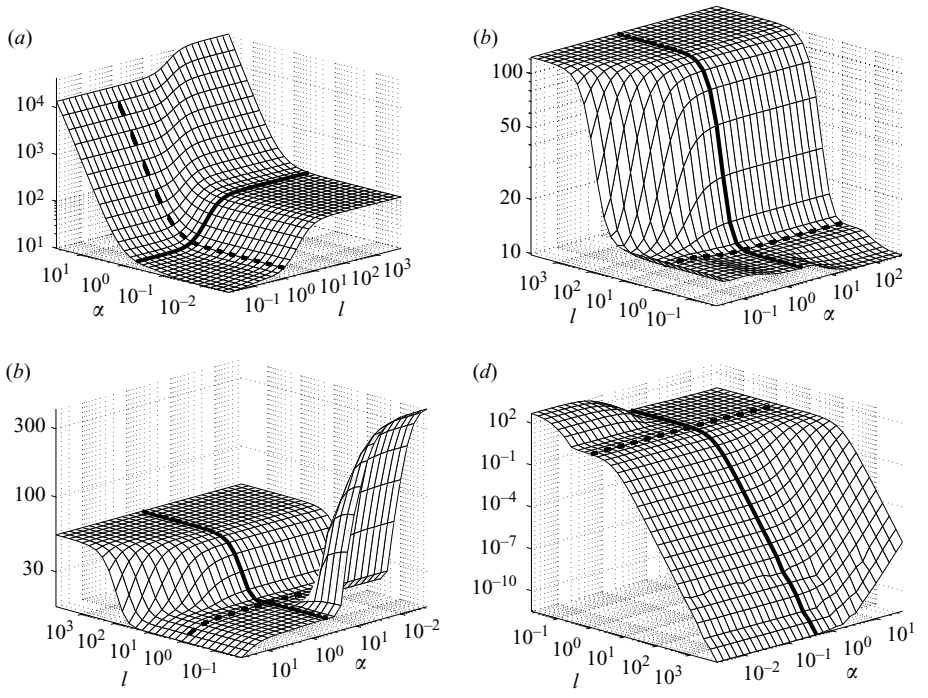

FIGURE 10. Magnitude of the objective functional and its various components as a function of mean energy weight α and control cost l. (a) Objective functional $\mathscr{I}$, (b) energy amplification $E(T_c)/E(0)$, (c) mean energy $(1/T_c)\int_0^{T_c} E(t)\,\mathrm{d}t$, ($d$) control energy $\langle\langle \boldsymbol{q}_w, \boldsymbol{q}_w \rangle\rangle$. Along the thick solid line, α is equal to 0.5 and along the thick dashed line, l is equal to 1. The parameters have been set to $Re = 550$, $k = 0.25$, $T_p = 14.3$, $T_c = 14.3$.

As the control cost l increases along the thick solid line, wall-normal blowing or suction becomes too expensive when compared to the resulting gain in the mean energy or in the energy amplification. Beyond the cutoff value $l_{cut} \sim 2$, the control energy drops precipitously (figure 10d). Since very little energy is dedicated to control, the energy amplification (figure 10b) and the mean energy (figure 10c) are nearly the same as for the uncontrolled optimal perturbation.

The mean energy weight α has little influence on the control strategy besides suppressing high transient energy growth between $t = 0$ and T_c. As α increases along the thick dashed line from $\alpha = 0.5$ to $\alpha = 40$, the energy amplification $E(T_c)/E(0)$ remains unchanged (figure 10b). When α is very high ($\alpha \sim 40$) the mean energy $(1/T_c)\int_0^{T_c} E(t)\,\mathrm{d}t$ decreases only slightly (figure 10c), the dependence on l, however, is much stronger. Since the mean energy is almost constant with respect to α along the thick dashed line, the objective functional (figure 10a) grows nearly quadratically at large α, owing to its dominant term $(\alpha^2/2)(1/T_c)\int_0^{T_c} E(t)\,\mathrm{d}t$.

When both α and l are large, the $E(T_c)/E(0)$ term in the objective functional is negligible. In this case, the goal of the optimal control is not so much to damp the energy amplification at $t = T_c$, but rather to decrease the mean perturbation energy between $t = 0$ and T_c while balancing the control energy expenses. Even when the control cost parameter l is beyond the cutoff l_{cut}, the cost of transient energy growth between $t = 0$ and T_c may be so high that it is worth blowing at the wall (figure 10d) in order to decrease the mean energy between $t = 0$ and T_c (figure 10c). A decrease

in the energy amplification $E(T_c)/E(0)$ (figure 10*b*) can be observed as a consequence of the overall damping of the energy prior to T_c.

Three regimes are thus delimited by the thick lines in figure 10.

Case $\alpha \gg 0.5$: the primary goal of our control strategy, which was to damp the energy amplification at a given time $E(T_c)/E(0)$, is overruled by a strong weighting of the mean energy term $(1/T_c)\int_0^{T_c} E(t)\,\mathrm{d}t$ in the objective functional.

Case $\alpha \ll 0.5, l \ll 1$: unrealistic amounts of control energy can be spent to damp the energy amplification at time T_c. The resulting energy peaks between $t=0$ and T_c render such control strategies undesirable.

Case $\alpha \leqslant 0.5,\ l \gg 1$: the control is so expensive with respect to the expected gain in the energy amplification that wall-blowing is prohibited. The weak control efforts result in plateau (figures 10*b*, *c*) consistent with the uncontrolled case.

By choosing moderate values of α and l, such as $\alpha = 0.5,\ l = 1$, the energy amplification is efficiently damped with a reasonable amount of wall-normal blowing and suction; these parameter settings may be regarded as delivering both an attractive and realistic control strategy. In what follows, the parameters α and l are set to $\alpha = 0.5$ and $l = 1$, and the manipulation of the underlying physical mechanisms under the corresponding control strategy is investigated.

6.2. *Physical mechanisms*

The effect of optimal control on the dynamics of initial disturbances at $Re = 2000$ is now examined from a physical point of view. Weight parameters have been set equal to $\alpha = 0.5$ and $l = 1$. A parameter study indicates that such values of α and l also yield an efficient control strategy at $Re = 2000$. Snapshots of the evolution of the optimal perturbation, as control is applied, are depicted in figures 11 and 12 and should be compared to the corresponding figures 7 and 8. A new layer of vortices confined to the wall is detected which travels with the naturally occurring vortices; the latter are observed to tilt more rapidly. In the wavenumber regime where vortex dipoles are not observed naturally (figure 8), vortex dipoles may be introduced by the control (figure 12). For wavenumbers at which vortex dipoles occur naturally, blowing and suction at the wall tend to accelerate this process (figure 11).

Transient vortex compression due to the spanwise shear is inevitable since the initial vorticity distribution inclined against the shear must evolve into the least stable eigenmode configuration where the vorticity distribution is inclined in the direction of the shear. Moderate wall-normal blowing or suction, obtained with $\alpha = 0.5$ and $l = 1$, is unable to prevent this tilting process. However, the associated transient energy growth may be weakened by accelerating the disturbance evolution into the least stable eigenmode. Using this acceleration strategy, disturbances are given less time to extract energy from the basic flow; hence, not only the energy at $t = T_c$, but also the energy maximum between $t = 0$ and T_c are decreased.

6.3. *Constant gain feedback control*

The optimal control strategy designed above requires the computation of the flow evolution from $t = 0$ to T_c several times, which may be computationally prohibitive for implementation in a real experiment. A more realistic, constant-gain feedback control strategy can be devised which performs nearly as well as optimal control at a much lower computational cost.

Assuming that a sensor is located at a distance y_m from the wall, we can design a control law of the form

$$v_w(t) = \kappa v(y_m, t), \tag{6.1}$$

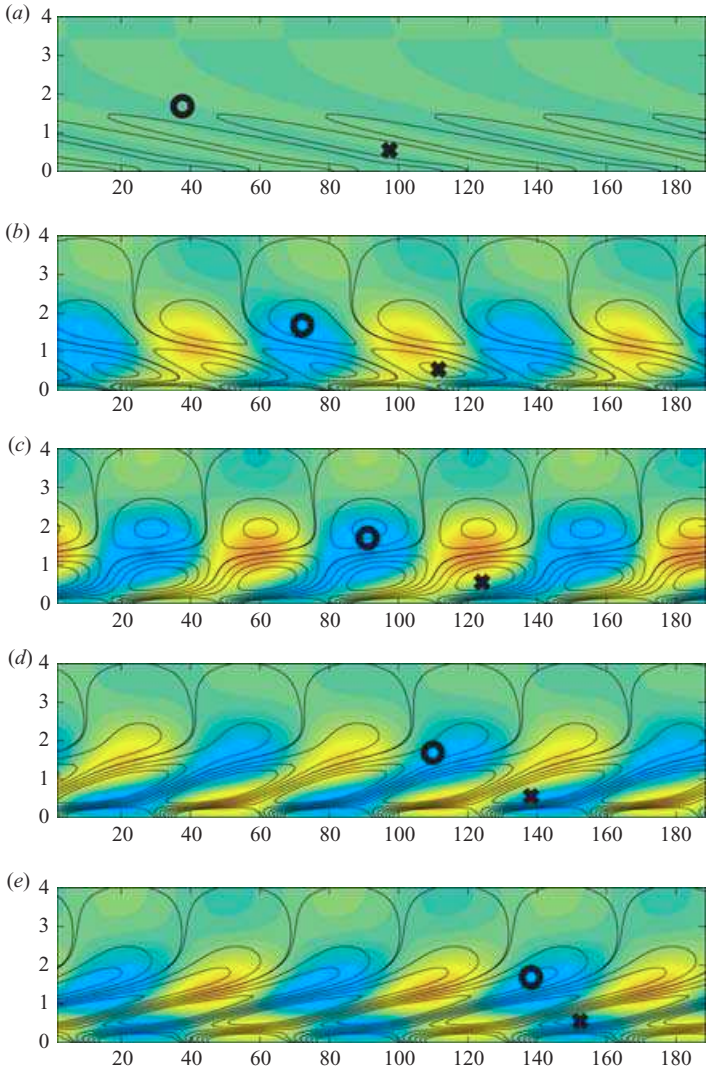

FIGURE 11. Time evolution of the overall optimal perturbation with optimal control applied, displayed in snapshots of the perturbation field in the (z, y)-plane over three spanwise wavelengths, at times (a) $t=0$, (b) $T_c/3$, (c) $2T_c/3$, (d) T_c, (e) $4T_c/3$. The sweep W is from left to right. The same field variables as in figure 7 are represented and the contour levels and the colour map are the same. The optimization time T_c has been set to $T_p = T_{max} = 12.9$ and the other parameters have been set to $Re = 2000$, $k = 0.1$, $\alpha = 0.5$ and $l = 1$. Vortex splitting occurs between (b) and (c), which should be compared to the uncontrolled case in figure 7 when vortices split between (c) and (d).

where κ is a constant scalar gain and $v(y_m, t)$ is the wall-normal velocity measured at the height y_m from the wall. The gain κ and the height y_m can be tuned so as to minimize the objective functional (3.1). By setting $\kappa = 0.6$ and $y_m = 1.8$, the objective functional is decreased to $\mathscr{I} = 21.8$ in the linearly stable case $Re = 550$, $k = 0.25$, which should be compared to $\mathscr{I} = 18.9$ when optimal control is applied. In the linearly unstable case $Re = 850$, $k = 0.25$, the constant gain control strategy with

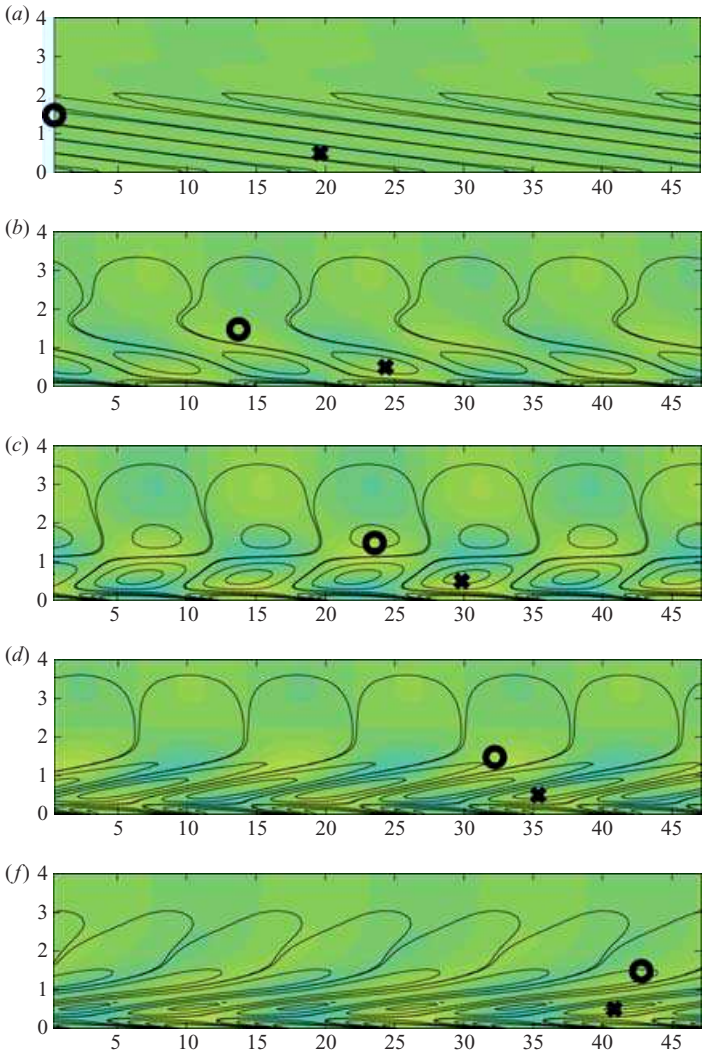

FIGURE 12. Same as figure 11 for $Re = 2000$, $k = 0.4$, $T_c = T_{max} = 22.2$, $\alpha = 0.5$ and $l = 1$. Vortex splitting is observed between (*b*) and (*c*), while in the uncontrolled case in figure 8, the vortices do not split.

$\kappa = 0.6$ and $y_m = 1.6$ yields $\mathscr{I} = 35.2$ whereas optimal control decreases the objective functional to $\mathscr{I} = 32.7$.

Figure 13 displays the wall-blowing and suction sequences for constant gain and optimal control. In both the linearly stable and unstable case, the wall-blowing pattern takes the form of travelling waves which follow the vortical structures. The spatio-temporal evolution of the control pattern displays a nearly perfect phase match between both control sequences in time and space which also have amplitudes of the same order. This observation shows that constant-gain feedback control provides a good approximation to the optimal control strategy.

The disturbance energy evolution with time is displayed in figure 14. The perturbations are efficiently damped by the constant-gain feedback control (6.1) both for linearly stable and linearly unstable flow. The energy peak transiently reached

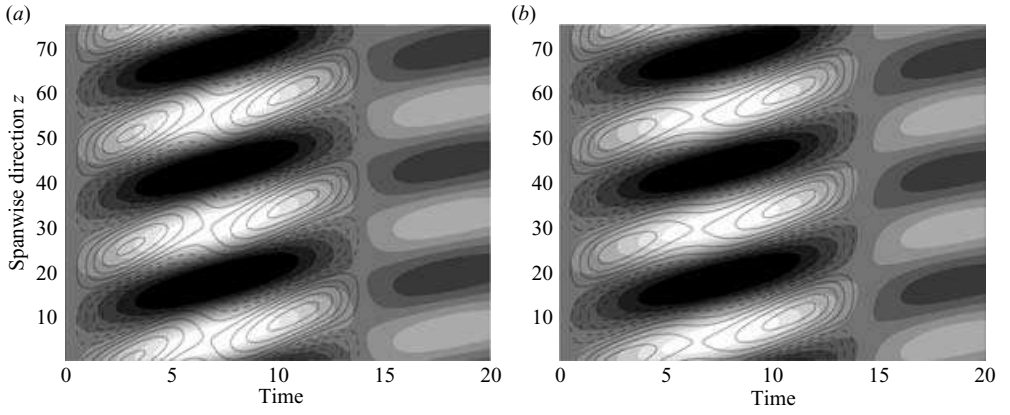

FIGURE 13. Isocontours of the wall-normal velocity v_w at the wall in the (t, z)-plane for (a) linearly stable ($Re = 550,\ k = 0.25$) and (b) linearly unstable ($Re = 850,\ k = 0.25$) flow. Shaded contours represent constant gain control (light: blowing; dark: suction) whereas line contours represent optimal control (solid lines: blowing; dashed lines: suction). The constant gain and the location of the sensor have been set to $(a)\ \kappa = 0.6,\ y_m = 1.8$, $(b)\ \kappa = 0.6,\ y_m = 1.6$ in order to minimize the objective functional $\mathscr{I}$. The remaining parameters have been set equal to $T_p = 14.3,\ T_c = 14.3,\ \alpha = 0.5,\ l = 1$.

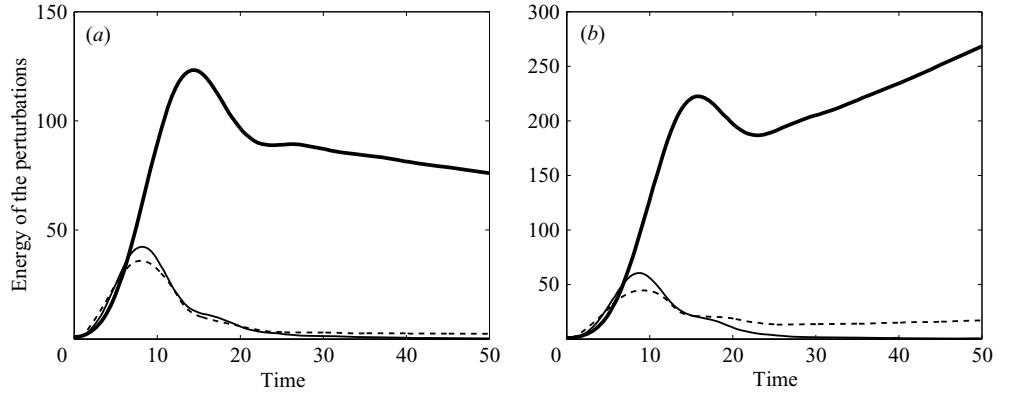

FIGURE 14. Disturbance energy as a function of time for (a) linearly stable ($Re = 550,\ k = 0.25$) and (b) linearly unstable ($Re = 850,\ k = 0.25$) flow. The thick solid line represents the uncontrolled optimal perturbation. The thin solid line displays the energy of the same perturbation when constant gain control is applied, the dashed line its counterpart when optimal control is applied. The constant gain and the location of the sensor have been set to $(a)\ \kappa = 0.6,\ y_m = 1.8$, $(b)\ \kappa = 0.6,\ y_m = 1.6$ in order to minimize the objective functional $\mathscr{I}$. The remaining parameters have been set equal to $T_p = 14.3,\ T_c = 14.3,\ \alpha = 0.5,\ l = 1$.

between $t = 0$ and $T_c = 14.3$ is of the same order of magnitude with both control strategies.

Even though the gain κ and the sensor location y_m have been tuned to minimize the objective functional $\mathscr{I}$ only on a finite-time interval, simulations show that the linearly unstable flow is stabilized for large times; after a short transient amplification the perturbation energy decreases exponentially as long as control is applied (figure 14b). The decay rate of the disturbance energy in the linearly stable case (figure 14a) is enhanced by constant-gain control.

The numerical experiments indicate that constant-gain feedback control is able to decrease the objective functional $\mathscr{I}$ very efficiently at a rather low computational cost when suitably tuned, and that it restabilizes linearly unstable perturbations in the long term. By contrast, evaluating the objective functional gradient requires the computation of the direct and adjoint problems from $t=0$ and T_c, which is computationally expensive; this computation also loses accuracy as T_c becomes large. Thus, the advantage of optimal control over constant-gain feedback control may be lost for long-term optimizations. Constant-gain feedback control strategies should, therefore, not be hastily discarded, but rather be considered as a viable option for controlling swept attachment-line boundary layers under realistic conditions.

7. Concluding remarks

An adjoint-based optimization procedure applicable to both the determination of the optimal perturbation and its optimal control has been developed, which relies on the introduction of a Lagrangian functional in the reduced $u-v$ setting (2.8)–(2.10). Although the formulation bears similarities to the previous investigations of Andersson *et al.* (1999) and Corbett & Bottaro (2001*a*, *b*), essential modifications have been introduced as outlined in § 3. In addition to the three scalar products (3.6*a*)–(3.6*c*), the double-bracketed scalar product (3.3) must be defined in order to express the kinetic energy of the perturbations in terms of the (u, v) components only. Had the analysis been conducted in primitive variables u, v, w, p, the scalar product (3.3) would have been superfluous and the usual Eulerian scalar product would have been sufficient. In the reduced $u-v$ setting, however, its double-bracketed counterpart (3.3), which takes into consideration the continuity equation, has to be used both to calculate the kinetic energy and the gradient of the objective functional. Provided attention is given to these points, the gradients of the objective functional readily follow from the Lagrangian formulation.

Two-dimensional (y, z)-mechanisms in the flow-dividing plane have been demonstrated (§ 5) to be responsible for most of the energy amplification of Görtler–Hämmerlin perturbations in swept Hiemenz flow. They involve spanwise-travelling vortices aligned in the chordwise direction that undergo a tilting of their vorticity distribution reminiscent of the Orr mechanism (Haynes 1987; Vanneste 1999): the vorticity distribution, initially inclined against the sweep, is compressed by the shear, which causes the associated energy to increase transiently before it eventually decreases exponentially (for the linearly stable case) or increases exponentially (for the unstable case). The growth of optimal perturbations exhibits two essential features that are specific to the swept attachment-line boundary layer. First, the transient growth does not rely on a lift-up process (Landahl 1980) as in classical boundary layers, but on tilting of the vorticity distribution induced by the spanwise shear. Secondly, the resulting chordwise vortices are distorted by the basic flow to form dipole structures which, at low spanwise wavenumbers, result in increased levels of spanwise velocity perturbations. These issues are discussed in more detail below.

The lift-up mechanism associated with streamwise momentum transport by vortices aligned with the flow is primarily responsible for the energy amplification in weakly non-parallel shear flows (Schmid & Henningson 2001). In the present study, the Görtler–Hämmerlin assumption does not allow for chordwise modulations of the spanwise velocity w, thus precluding any lift-up associated with the spanwise shear $W'(y)$. The optimal perturbation has been shown to consist of chordwise vortices aligned with the chordwise shear $\partial U/\partial y(x, y)$. However, according to figure 15(*a*),

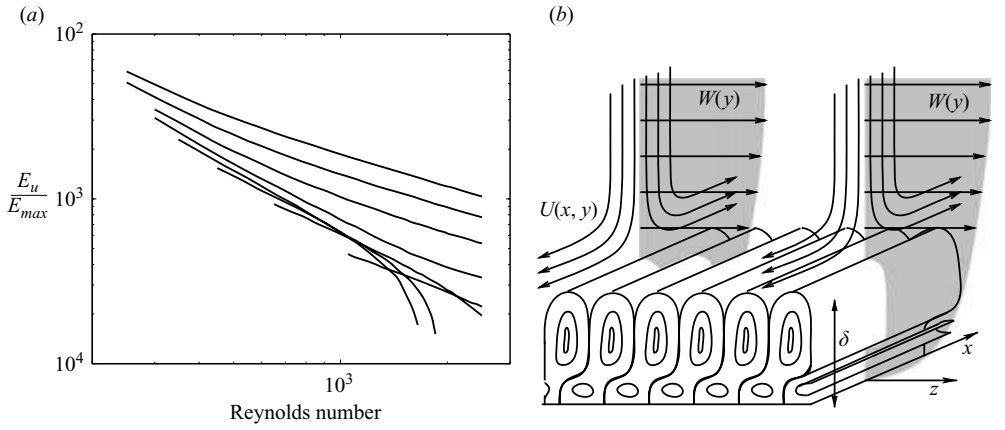

FIGURE 15. (*a*) Fraction of the chordwise velocity perturbation energy $\int_0^\infty u^* u \, \mathrm{d}y$ in the maximum total energy $E(T_{max})$ reached by optimal perturbations versus Reynolds number. Spanwise wavenumbers range from $k = 0.45$ (top curve) to $k = 0.1$ (bottom curve) in 0.05 increments. (*b*) Sketch illustrating the inefficiency of 'laterally swept' lift-up. The up- and down-welling regions aligned in the chordwise direction x work in opposition as they are swept in the z-direction.

lift-up effects associated with the chordwise shear $\partial U/\partial y(x, y)$ are weak: the maximum kinetic energy of the chordwise velocity perturbation, $\int_0^\infty u^* u \, \mathrm{d}y$, accounts for only one-thousandth of the total maximum energy amplification $E(T_{max})$ reached by optimal disturbances.

In contrast to weakly non-parallel boundary layers, the chordwise vortices involved in the lift-up mechanism are advected in the spanwise direction by the sweep W (figure 15*b*); as a result, they do not coherently transport low-momentum fluid from the wall to the edge of the boundary layer and high-momentum fluid from the boundary layer toward the wall. Rather, up- and down-welling regions work in opposition as they are swept along the attachment-line. Figure 15(*a*) further illustrates the role of the basic sweep velocity in rendering the chordwise lift-up mechanism ineffective: higher Reynolds numbers, i.e. larger sweep velocities, lead to lower chordwise disturbance energy when compared to the total energy achieved by optimal perturbations. The only remaining amplification processes are therefore the Orr mechanism and vortex dipole formation.

The combined action of the spanwise shear $W'(y)$ and the compression by the impinging basic flow results in the tilting of the chordwise vorticity distribution and in the compression of the chordwise vortices into dipole structures, respectively. This process is the most effective at large spanwise wavelengths (low k) which allow for more elongated initial vorticity distributions. The vortices are confined to the spanwise boundary layer, the thickness of which is constant. When k is decreased below $k \sim 0.25$, vorticity patches can no longer be tilted up by the basic shear and remain inside the boundary layer without undergoing vortex splitting (figure 7). When k is above 0.25, the process is incomplete: vortices are merely distorted and dipolar structures are not observed (figure 8). The optimal wall blowing/suction sequence which has been shown to resemble constant gain feedback control (§ 6.3), enhances the above compression process by pushing the vortices against the impinging flow.

The present study was aimed solely at describing Görtler–Hämmerlin disturbances near the attachment-line within the context of the idealized swept Hiemenz flow model.

The optimal growth of arbitrary disturbances in swept Hiemenz flow remains to be determined: according to the studies of Theofilis *et al.* (2003) and Obrist & Schmid (2003*b*), higher-order chordwise polynomial expansions may be expected to (*a*) yield stronger amplifications than Görtler–Hämmerlin perturbations and (*b*) introduce additional unstable modes. The stronger growth is caused by the superposition of modes with very similar wall-normal shapes (Obrist & Schmid 2003*b*). The additional unstable modes, although less unstable than Görtler–Hämmerlin modes, may compromise the efficiency of constant-gain feedback control schemes which are unable to stabilize multiple modes.

Moreover, the precise relationship between the present spanwise travelling chordwise vortices generated by transiently amplified or genuinely unstable perturbations at the attachment-line and the steady crossflow vortices produced in the three-dimensional boundary layer on the wing surfaces (Arnal, Coustols & Juillen 1984; Bertolotti 1999; Koch *et al.* 2000, among others) remains to be determined.

The authors gratefully acknowledge many enlightening and productive discussions with Carlo Cossu and François Gallaire. A. G. holds a PhD fellowship from CNRS and the French 'Délégation Générale pour l'Armement'. P. J. S. 's stay at LadHyX was supported financially by the CNRS.

REFERENCES

Abergel, F. & Témam, R. 1990 On some control problems in fluid mechanics. *Theoret. Comput. Fluid Dyn.* **1**, 303–325.

Andersson, P., Berggren, M. & Henningson, D. S. 1999 Optimal disturbances and bypass transition in boundary layers *Phys. Fluids* **11**, 134–150.

Arnal, D., Coustols, E. & Juillen, J. C. 1984 Etude expérimentale et théorique de la transition sur une aile en flèche infinie. *La Recherche Aérospatiale* **4**, 275–290.

Bertolotti, F. P. 1999 On the connection between cross-flow vortices and attachment-line instabilities. In *Proc. of the IUTAM Symp. on Laminar–Turbulent Transition, Sedona.*

Bewley, T. R. 2001 Flow control: new challenges for a new Renaissance. *Prog. Aerospace Sci.* **37**, 21–58.

Bewley, T. R. & Liu, S. 1998 Optimal and robust control and estimation of linear paths to transition. *J. Fluid Mech.* **365**, 305–349.

Bewley, T. R., Moin, P. & Temam, R. 2001 DNS-based predicitive control of turbulence: an optimal benchmark for feedback algorithms. *J. Fluid Mech.* **447**, 179–225.

Brattkus, K. & Davis, S. H. 1991 The linear stability of plane stagnation-point flow against general disturbances. *Q. J. Mech. Appl. Maths* **44**, 135–146.

Butler, K. M. & Farrell, B. F. 1992 Three-dimensional optimal perturbations in viscous shear flow. *Phys. Fluids* A **4**, 1637–1650.

Cathalifaud, P. & Luchini, P. 2000 Algebraic growth in boundary layers: optimal control by blowing and suction at the wall. *Eur. J. Mech.* B *Fluids* **19**, 469–490.

Corbett, P. & Bottaro, A. 2001*a* Optimal linear growth in swept boundary layers. *J. Fluid Mech.* **435**, 1–23.

Corbett, P. & Bottaro, A. 2001*b* Optimal control of nonmodal disturbances in boundary layers. *Theoret Comput Fluid Dyn.* **15**, 65–81.

Cumpsty, N. A. & Head, M. R. 1969 The calculation of the three-dimensional turbulent boundary layer. Part III: Comparison of attachment-line calculations with experiment. *Aero. Q.* **20**, 99–113.

Dhanak, M. R. & Stuart, J. T. 1995 Distortion of the stagnation-point flow due to cross-stream vorticity in the external flow. *Phil. Trans. R. Soc. Lond.* A **352**, 443–452.

Gad-el-Hak, M. 2000 *Flow Control: Passive, Active, and Reactive Flow Management*. Cambridge University Press.

Gaster, M. 1967 On the flow along swept leading edges. *Aero. Q.* **18**, 165–184.

Görtler, H. 1955 Dreidimensionale Instabilität der ebenen Staupunktsströmung gegenüber wirbelartigen Störungen. In *50 Jahre Grenzschichtforschung*. (ed. H. Görtler & W. Tollmien). Vieweg, Braunschweig.

Greenbaum, A. 1997 *Iterative Methods for Solving Linear Systems*. SIAM, Philadelphia.

Gregory, M. A. 1960 Transition and the spread of turbulence on a 60° swept-back wing. *J. R. Aero. Soc.* **64**, 562.

Gunzburger, M. D. 1995 *Flow Control*. The Institute for Mathematics and Its Applications, vol. **68**, Springer.

Gunzburger, M. D. 1997 *Inverse Design and Optimization Methods*. Von Karman Institute for Fluid Dynamics Lecture Series 1997-05.

Gustavsson, L. H. 1991 Energy growth of three-dimensional disturbances in plane Poiseuille flow. *J. Fluid Mech.* **224**, 241–260.

Hall, P. & Malik, M. R. 1986 On the instability of a three-dimensional attachment-line boundary layer: weakly nonlinear theory and a numerical approach. *J. Fluid Mech.* **163**, 257–282.

Hall, P., Malik, M. R. & Poll, D. I. A. 1984 On the stability of an infinite swept attachment line boundary layer. *Proc. R. Soc. Lond.* A **395**, 229–245.

Hämmerlin, G. 1955 Zur Instabilitätstheorie der ebenen Staupunktsströmung. In *50 Jahre Grenzschichtforschung*. (ed. H. Görtler & W. Tollmien). Vieweg, Braunschweig.

Haynes, P. H. 1987 On the instability of sheared disturbances. *J. Fluid Mech.* **175**, 463–478.

Hiemenz, K. 1911 Die Grenzschicht an einem in den gleichförmigen Flüssigkeitsstrom eingetauchten geraden Kreiszylinder. PhD thesis, Göttingen.

Hill, D. C. 1995 Adjoint systems and their role in the receptivity problem for boundary layers. *J. Fluid Mech.* **292**, 183–204.

Högberg, M. & Henningson, D. S. 2002 Linear optimal control applied to instabilities in spatially developing boundary layers. *J. Fluid Mech.* **470**, 151–179.

Högberg, M., Bewley, T. R. & Henningson, D. S. 2003 Linear feedback control and estimation of transition in plane channel flow. *J. Fluid Mech.* **481**, 149–175.

Joshi, S. S., Speyer, J. L. & Kim, J. 1997 A systems theory approach to the feedback stabilization of infinitesimal and finite-amplitude disturbances in plane Poiseuille flow. *J. Fluid Mech.* **332**, 157–184.

Joslin, R. D. 1995 Direct simulation of evolution and control of three-dimensional instabilities in attachment-line boundary layers. *J. Fluid Mech.* **291**, 369–392.

Joslin, R. D. 1998 Aircraft laminar flow control. *Annu. Rev. Fluid Mech.* **30**, 1–29.

Joslin, R. D., Gunzburger, M. D., Nicolaides, R. A., Erlebacher, G. & Hussaini, M. Y. 1997 Self-contained automated mehodology for optimal flow control. *AIAA J.* **35**, 816–824.

Koch, W., Bertolotti, F. P., Stolte, A. & Hein, S. 2000 Nonlinear equilibrium solutions in a three-dimensional boundary layer and their secondary instability. *J. Fluid Mech.* **406**, 131–174.

Landahl, M. T. 1980 A note on an algebraic instability of inviscid parallel shear flows. *J. Fluid Mech.* **98**, 243–251.

Lin, R.-S. & Malik, M. R. 1996 On the stability of attachment-line boundary layers. Part 1. The incompressible swept Hiemenz flow. *J. Fluid Mech.* **311**, 239–255.

Luchini, P. 2000 Reynolds-number-independent instability of the boundary layer over a flat surface: optimal perturbations. *J. Fluid Mech.* **404**, 289–309.

Lumley, J. & Blossey, P. 1998 Control of turbulence. *Annu. Rev. Fluid Mech.* **30**, 311–327.

Lyell, M. J. & Huerre, P. 1985 Linear and nonlinear stability of plane stagnation flow. *J. Fluid Mech.* **161**, 295–312.

Obrist, D. & Schmid, P. J. 2003*a* On the linear stability of swept attachment-line boundary layer flow. Part 1. Spectrum and asymptotic behaviour. *J. Fluid Mech.* **493**, 1–29.

Obrist, D. & Schmid, P. J. 2003*b* On the linear stability of swept attachment-line boundary layer flow. Part 2. Non-modal effects and receptivity. *J. Fluid Mech.* **493**, 31–58.

Pfenninger, W. 1977 Laminar flow control – Laminarization. Special Course on Concepts for Drag Reduction. *AGARD* 654.

Pfenninger, W. & Bacon, J. W. 1969 Amplified laminar boundary layer oscillations and transition at the front attachment line of a 45 deg swept flat-nosed wing with and without suction. In *Viscous Drag Reduction* (ed. C. S. Wells), pp. 85–105. Plenum.

Poll, D. I. A. 1979 Transition in the infinite swept attachment line boundary layer. *Aero. Q.* **30**, 607–629.

Pralits, J. O., Hanifi, A. & Henningson, D. S. 2002 Adjoint-based optimization of steady suction for disturbance control in incompressible flows. *J. Fluid Mech.* **467**, 129–161.

Press, W. H., Teukolsky, S. A., Vetterling, W. T. & Flannery, B. P. 1992 Minimization or Maximization of Functions. In *Numerical Recipes in Fortran, chap. 10*. Cambridge University Press.

Protas, B., Bewley, T. R. & Hagen, G. 2004 A comprehensive framework for the regularization of adjoint analysis in multiscale PDE systems. *J. Comput. Phys.* **195**, 49–89.

Schmid, P. J. & Henningson, D. S. 2001 *Stability and Transition in Shear Flows*. Springer.

Spalart, P. R. 1988 Direct numerical study of leading-edge contamination. In *Proc. of the AGARD Symp. on Application of Direct and Large-Eddy Simulation to Transition and Turbulence*. AGARD CP-438.

Theofilis, V. 1998 On linear and nonlinear instability of the incompressible swept attachment-line boundary layer. *J. Fluid Mech.* **355**, 193–227.

Theofilis, V., Fedorov, A., Obrist, D. & Dallmann, U. C. 2003 The extended Görtler-Hämmerlin model for linear instability of three-dimensional incompressible swept attachment-line boundary layer flow. *J. Fluid Mech.* **487**, 271–313.

Trefethen, L. N., Trefethen, A. E., Reddy, S. C. & Driscoll, T. A. 1993 Hydrodynamic stability without eigenvalues. *Science* **261**, 578–584.

Vanneste, J. 1999 A spatial analogue of transient growth in plane Couette flow. *J. Fluid Mech.* **397**, 317–330.

Walther, S., Airiau, C. & Bottaro, A. 2001 Optimal control of Tollmien–Schlichting waves in a developing boundary layer. *Phys. Fluids* **13**, 2087–2096.

Wilson, S. D. R. & Gladwell, I. 1978 The stability of a two-dimensional stagnation flow to three-dimensional disturbances. *J. Fluid Mech.* **84**, 517–527.